Roman Svoboda (2024). Johnson-Mehl-Avrami kinetics as a universal description of crystallization in glasses?. *Journal of the European Ceramic Society*. Volume 44, Issue 6, June 2024, Pages 4064-4082. DOI: 10.1016/j.jeurceramsoc.2023.12.096

Johnson-Mehl-Avrami kinetics as a universal description of crystallization in glasses?

Roman Svoboda*

Department of Physical Chemistry, University of Pardubice, Studentska 573, 532 10 Pardubice, Czech Republic

Abstract

Applicability of the Johnson-Mehl-Avrami (JMA) model beyond the typical range of the negative asymmetries of the crystallization peak was tested by means of theoretical simulations. Using the solid-state kinetic equation with implemented temperature dependences of either activation energy E or pre-exponential factor A, it was shown that the originally monotonically increasing transformation rate constant changes its evolution with temperature to a non-monotonous course, exhibiting a broad maximum. If the crystallization process following the non-isothermal JMA kinetics proceeds near this maximum, the asymmetry of the corresponding kinetic peak can gradually change to significantly positive values. Of particular interest are the cases with the JMA kinetic exponent $m_{JMA} \geq 2$, where the asymmetry of the JMA peaks changes with increasing heating rate from the typical negative values to largely positive values – such crystallization behavior was indeed observed for several chemically diverse materials (polymers, small organic molecules, chalcogenide and oxide glasses).

Keywords: JMA model; extended applicability; theoretical simulation; asymmetry

* Corresponding author: Tel.: +420 466 037 346 E-mail address: roman.svoboda@upce.cz

1. Introduction

Glass-ceramics represent a class of materials that combines the transparency and amorphous nature of glasses with the crystallinity and mechanical properties of ceramics. [1 - 3] This unique combination of properties has led to a wide range of applications in various scientific and industrial fields. Glass-ceramics find extensive use in electronics and photonics due to their excellent optical properties, electrical insulation, and thermal stability. Their crystalline phase can be engineered to exhibit specific optical behaviors, making them suitable for lenses, prisms, and optical waveguides in communication devices and laser systems. [4 - 6] Moreover, their electrical insulating properties make them ideal substrates for integrated circuits and microelectromechanical systems (MEMS). [7 - 9] In the household and culinary industry, glass-ceramics find use as materials for cookware, stovetops and ovens; it is also used as thermal insulation, including fireplace doors and high-temperature insulating panels. [10, 11] In the dental and medical fields, the glass-ceramics are employed as materials for dental crowns, bridges, bone implants and other prosthetic devices – the Bioglass 45S5 is particularly well known in this regard. [12 - 15] Furthermore, the glass-ceramics materials play a pivotal role in nuclear waste immobilization and storage [16, 17]; in aerospace and aviation, they are utilized for components such as heat-resistant windows, thermal insulating tiles, and nozzle materials in rocket propulsion systems [18, 19]; in the automotive industry, the glass-ceramics can be used for catalytic converter substrates due to their ability to withstand high exhaust temperatures [20, 21].

Such large portfolio of technological applications naturally implies utilization of numerous material families for the preparation of the appropriate glass-ceramics. In correspondence to the massive variation of the structural, thermal and mechanical properties of these source glassy matrices, broad diversity of the crystallization behavior types is encountered during the efforts for controlled formation of the crystalline phase within the

parent glass. The key step for the successful preparation of glass-ceramics with required amount of contained crystallites is an accurate mathematical description of the crystallization process, based on which a precise kinetic prediction can be made. Nowadays, the crystallization kinetics is commonly described in terms of the standard derivative kinetic equation [22]:

$$d\alpha/dt = K(T)\cdot f(\alpha) = I \cdot A \cdot e^{-E/RT} \cdot f(\alpha) \tag{1}$$

where dα/dt is the amorphous-to-crystalline transformation rate, K is the kinetic rate constant, α is the degree of conversion, t is time, T is temperature, A is the pre-exponential factor, E is the apparent activation energy for the crystallization process, R is the universal gas constant (8.3145 $J \cdot mol^{-1} \cdot K^{-1}$), I is the integrated area under the kinetic peak (corresponding to the crystallization enthalpy), and $f(\alpha)$ is a substitute for a kinetic model. In contrast to the large variety of different types of nucleation and crystal growth mechanisms [23 - 25], the macroscopic crystallization kinetics is usually described in terms of only two solid-state kinetic models f(α): the physically meaningful nucleation-growth Johnson-Mehl-Avrami-(Kolmogorov), JMA(K), model [26 - 30] (see Eq. 2) and the empirical autocatalytic Šesták-Berggren, AC, model [31] (see Eq. 3).

$$f(\alpha) = m(1-\alpha)[-\ln(1-\alpha)]^{1-(1/m)} \tag{2}$$

$$f(\alpha) = \alpha^{M}(1-\alpha)^{N} \tag{3}$$

The quantities m, M and N in the equations shown above correspond to the kinetic exponents (material "constants") of the JMA and AC models – note that the abbreviation JMA will be used in the present paper as it is the most common one .

The main advantage of the JMA model over the AC model is, obviously, its physico-chemical background, which relates the JMA kinetic exponent m with the information about the dimensionality of the growing crystallites, and about the potential simultaneous progress of the nucleation process. This benefit is compensated by the relatively strict rules for the

applicability of the JMA model. In particular, only crystallization peaks exhibiting certain asymmetry may correspond to the JMA kinetics – note the recent update [32] regarding the limits of the JMA model applicability expressed by the simple metrics of the masterplot function z(α) (Eq. 4), where the degree of conversion corresponding to the maximum of the z(α) function $\alpha_{max,z}$ was correlated to the theoretically simulated JMA data.

$$z(\alpha) = \frac{d\alpha}{dt} \cdot T^2 \tag{4}$$

Based on the correlation coefficients associated with the fit by the JMA model, the following borderline asymmetries corresponding to the JMA kinetics were determined: $\alpha_{max,z}$ = 0.620 – 0.665 results in the correlation coefficient r^2 = 0.999, and $\alpha_{max,z}$ = 0.585 – 0.705 corresponds to r^2 = 0.995. [32] Although these limits significantly extend the JMA model applicability compared to the previous (only vaguely and imprecisely defined) state of matters, the constraints still provide a relatively narrow window for the JMA model applicability and, in practice, majority of the crystallization data still needs to be described by the empirical AC model. This is demonstrated in Fig. 1A, where the required JMA asymmetries of the derivative kinetic peaks (as defined by the findings from [32]) are depicted together with two cases of borderline asymmetries encountered for the crystallization kinetic peak in practice (the data were simulated using the combination of Eqs. 1 + 3 to cover all typical asymmetries of the crystallization peak; the high narrow kinetic peak skewed to higher T exhibits highly negative asymmetry, and the small broad kinetic peak skewed to lower T exhibits higly positive asymmetry).

Since the commonly used flexible AC model does not provide relevant information regarding the physico-chemical background of the crystallization process (although the model is still highly relevant for the main goal of the kinetic analysis, i.e., the kinetic predictions), a high incentive exits for the scientists to incorporate the physically meaningful JMA model (very often incorrectly) into almost every evaluation of the crystallization kinetic data. The

easiest preliminary verification of the JMA model applicability is based on the limits for the $\alpha_{max,z}$ value (as described above and in greater detail in [32]); the ultimate confirmation would then be direct fit of the derivative experimental data (see Fig. 1) by the combination of Eqs. 1and 2. But is this approach really universal, with no exceptions? Or is there a situation, when e.g. a crystallization peak with positive asymmetry could still be in agreement with the JMA kinetics?

The two main premises for the derivation of the findings presented in [32] were:

1) the crystallization occurs by means of a single process.
2) the crystallization process exhibits a uniform growth mechanism with the model-free quantities (E and A in Eq. 1) being material constants.

Regarding the first premise, it was shown in [33] that no combination of two JMA processes (overlapping to such a degree that the overall derivative signal is perceived as a single peak) can result in a signal with positive asymmetry – the overall asymmetry of the two closely overlapping JMA peaks can shift slightly outside of the limits introduced in [32] but the fact that the signal consists of two underlying/overlapping sub-processes is always revealed during the consequent direct of the experimental data by the JMA model (Eqs. 1 + 2). On the other hand, the second premise is not always fulfilled, as the activation energy changes with T or applied heating rate q^+ relatively frequently. [34 - 40] The temperature-dependent E (and/or A) can be approximated and implemented in the kinetic calculations by using the recently developed single-curve multivariate kinetic analysis (sc-MKA) method [41]. However, this methodology primarily provides results reflecting the dominant effect of changing q^+ (i.e. associated with e.g. time provided for the nucleation) but does not contain the mathematics incorporating the temperature-dependent E and/or A into the kinetic description of each individual data-curve. Withal, it is this kinetic effect that intrinsically changes the asymmetry

of the kinetic peak and could be responsible for a potentially extended applicability of the JMA model outside of its currently considered boundaries.

In the present paper, the effect of the temperature-dependent activation energy E and pre-exponential factor A on the changes of the JMA asymmetry will be explored. Theoretical simulations will be used to demonstrate that the incorporation of E(T) and A(T) into Eq. 1 will cause the JMA kinetics to produce more symmetric (and even positively asymmetric) kinetic peaks. Three main metrics (the evaluation of which is depicted in Fig. 1B) will be used to consider the skewing of the simulated kinetic peaks with E(T) and A(T), and to enumerate their asymmetries: 1) the $\alpha_{max,z}$ (resulting from Eq. 4) – see Fig. 1B for the JMA z(α) function with its maximum corresponding to $\alpha_{max,z}$ = 0.632; 2) the asymmetry factor AF (defined by Eq. 5 applied to distances "a" and "b" in 1/10 of the peak height); 3) the tailing factor TF (defined by Eq. 6 applied to distances "a" and "b" in 1/20 of the peak height). Note that all three metrics are dimensionless.

$$AF = \frac{b}{a} \tag{5}$$

$$TF = \frac{(a+b)}{2a} \tag{6}$$

2. Results

A standard series of the JMA kinetic peaks simulated at different heating rates q^+ by combination of Eqs. 1 + 2 is depicted in Fig. 2A. For such case, E and A are considered material constants in the whole relevant temperature range, and the rate constant K exponentially increases with T – see Fig. 2C. The above-defined metrics for the standard JMA kinetics are: $\alpha_{max,z}$ = 0.632, AF = 0.53, TF = 0.74. On the other hand, only by introducing temperature dependent activation energy E(T) (and thereby forcing also A(T)), the JMA kinetic peaks are skewed, and can exhibit even positive asymmetry – see Fig. 2B. The primary E(T) and A(T) inputs were inspired by the recent crystallization data obtained

experimentally for the CeO_2-doped Bioglass 45S5 for medical applications [42]. Note however, that all present data are fully theoretically simulated and will always exactly correspond to the JMA kinetic concept, which will only be modified by adding the temperature dependent E (and as a consequence A). The experimental data from [42] were used to set the initial E and A ranges, so that the present simulations realistically reflect the potential real-life crystallization processes (this will be further discussed in section 3). The E(T) and A(T) dependences corresponding to Fig. 2B are depicted in Fig. 2D. The fundamental background behind the change of the shape of the kinetic peaks lies in the non-monotonous temperature dependence of the rate constant K, which occurs as a direct mathematical consequence of E and A decreasing with T. [34 - 40] This course of the K-T dependence (see Fig. 2D) very closely imitates the fact that for the real materials, the microscopic crystal growth rate also always exhibits a maximum (below the melting point T_m) [43], which is the result of competing influences of the increasing driving force (increases with undercooling ΔT) and decreasing diffusion (decreases with temperature) [44]. Technically, qualitatively identical situation can thus occur for all glassy materials, if appropriate conditions are reached. In practice, this is of course not always possible, as the crystal growth needs to occur across a large T range associated with sufficient K change (many materials crystallize within the initial region characterized by the exponential K increase with T). Nonetheless, as was shown e.g. in [45], even the rapidly crystallizing phase-change Ge-Sb-Te materials can exhibit similar behavior and skewing of the JMA crystallization kinetic peaks, when heated by using the fast-scanning calorimeter FSC [46]. This indicates that the T-dependent JMA kinetics may be significantly more prevalent than perceived based on the standard methods of kinetic analysis [47], and possibly even universally applicable to an absolute majority of crystallization processes.

In the following sub-sections, the influence of the E(T) and A(T) parametrizations on the intensity of the kinetic peaks skewing will be explored. The mathematical function expressing the E(T) dependences was chosen in accordance with the experimentally observed curvatures [34 - 40] expressed by the well-known linearizing Kissinger method [48]:

$$\ln\left(\frac{q^{+}}{T_p^2}\right) = -\frac{E}{RT_p} + const. \tag{7}$$

where T_p stands for the temperature corresponding to the maximum of the kinetic peak. For the T-dependent E, the Kissinger dependence of $\ln(q^{+}/T_p^2)$-T^{-1} is fit by the second-order polynomial equation to account for its curvature (as is the practice for the real-life data, where this polynomial describes the curvatures with high correlation coefficient):

$$Y = P1 \cdot X^2 + P2 \cdot X + P3 \tag{8}$$

where P1, P2 and P3 are constants. The E-T dependence is then calculated as (which results from the derivation of combined Eqs. 7 and 8):

$$E(T) = R \cdot \left(2 \cdot P1 \cdot \frac{1}{T} + P2\right) \tag{9}$$

Regarding the A-T dependence, it is dictated by the so-called compensation effect [49] for the real-life data, which for the present simulations translates into a linear log$A$-T^{-1} dependence. For the following sub-sections, the A(T) dependence will be characterized by Eq. 10:

$$\log A(T) = 45.673 \cdot \frac{1}{T} + 28.628 \tag{10}$$

which is based on the results obtained for the CeO_2-doped Bioglass 45S5 [42]; the only exception will be the sub-section 2.3., where the influence of the T-dependent pre-exponential factor on the JMA kinetics will be demonstrated (the above-described choice will be justified). Note that the initial selection of the parameters for Eqs. 9 and 10 were done on the basis of the real experimental data [42], so that the consequent simulations were done within reasonable boundaries, close to what can be encountered in practice. The consequent

variations of these parameters were arbitrary choices covering various cases of significantly different E-T dependences.

2.1. Influence of the E-T curvature

The first explored effect is that associated with the curvature of the E-T dependence. In order to preserve the initially set characteristics of the JMA data (based on [42]), the following enumeration of Eqs. 1 +2 was applied: A characterized by Eq. 10, I = 1, m_{JMA} = 1. Five different E(T) dependences were implemented in accordance with Eq. 9 and the following combinations of the P1&P2 parameters: -55&60, -50&51, -45&43, -40&34, and -35&25. The corresponding simulated sets of JMA peaks and the E-T dependences themselves are shown in Fig. 3. As can be seen in this figure, the initial decrease of curvature (-55&60 → 50&51) quite significantly enhanced the skew of the kinetic peaks simulated across the chosen q^+ span (0.5 – 50 °C·min^{-1}). The further decreases of the E-T curvature resulted in only minor changes in the peaks skew. This effect is associated with the overall E value decreasing in the T range initially surpassed by the crystal growth process, which leads to a shift of the kinetic peak to lower temperatures in a similar fashion as is exhibited by the K-T dependence (see Supplemental online material for the corresponding simulated K-T data, which get narrower and shift to lower T with decreasing E-T curvature). As such, the main portion of the crystal growth process proceeds in a similar section of the K-T dependence, resulting in a similar kinetic response – see Figs. 3B – 3E.

The corresponding pre-defined metrics for the peaks asymmetry (Eqs. 4 – 7) are displayed in Fig. 4. Let us start with the most well-known figure, the Kissinger plot (Fig. 4A). The Kissinger dependences are for the standard JMA kinetics perfectly linear. However, these dependences are for the JMA model with implemented E-T dependence clearly curved, indicating the non-constant value of activation energy. It is noteworthy that the deviation of

the Kissinger dependence from its linear trend set by the data-points obtained at the lowest q^+ translates into the temperature shift of T_p by $\Delta T_p \approx 17 - 18$ °C at 20 °C·min^{-1}, which is consistent with the ΔT_p magnitudes obtained experimentally – see e.g. [34 - 42]. The universal asymmetry factors, AF and TF (see Eqs. 5 and 6, and Figs. 4C and 4D), show a very large increase corresponding to the major change from the negatively asymmetric to the positively asymmetric kinetic peaks – the ideally symmetric peaks are in cases of both factors characterized by the value 1. Worth noting are also the deviated data-points evaluated for $q^+ =$ 50 °C·min^{-1}, where under certain conditions E decreases to extremely low values, which causes mathematical cease of further process continuation (α stagnates at value < 1) – signs of such behavior can also be rarely encountered for real-life crystallization data. Finally, the $\alpha_{max,z}$ values determined for the present sets of simulated JMA peaks are shown in Fig. 4D. Considering that the lower limits of the standard JMA kinetics (with no E(T) implemented) applicability are 0.620 and 0.585 for the $r^2 = 0.999$ and $r^2 = 0.995$, respectively, [32] a majority of the JMA kinetic peaks skewed due to the implemented E-T dependence would be under standard circumstances [47] evaluated as non-conformable with the JMA kinetics. This apparent discrepancy evidently opens up a large unexplored field of kinetic scenarios that may explain the long time experimentally observed T- and q^+-dependent crystallization kinetics [34 - 42] manifesting as various clear trends in the kinetic parameters such as E, A, I, m_{JMA}, or even M and N from the AC model.

2.2. Influence of the absolute E magnitudes in the E-T dependence

As the second investigated effect, the magnitude of the absolute E values within the E-T dependence (i.e. the sole influence of P2) was tested. The theoretical simulations of the JMA data were based on the similar sets of kinetic parameters; the following combinations of the P1&P2 parameters were used: -55&60, -55&65, -55&70, -35&25, -35&30, and -35&35.

As is apparent from Fig. 5, the decrease of E (i.e. the shift of the overall E-T dependence to lower E values) causes a significant cease of the skewing effect in all tested cases. Note that the testing was done for the two borderline curvatures introduced in section 3.1., which means that the cease of the skew is universal for all curvatures shown in Figs. 3 and 4. The degree of skewing decreases with the decreasing E (increasing P2); the first decrease of E has the most prominent ceasing effect, and the further decreases of E influence the skewing progressively less. The underlying mathematics behind the kinetics changes depicted in Fig. 5 is based on the rather minor shifts of the K-T dependences (see Supplemental online material), where the dominant change of E (see Fig. 6A) is not balanced by a corresponding change of A. This leads to the crystallization process being localized more towards the onset edge of the K-T peak lower T), where only small skewing takes place.

The loss of skewing is naturally reflected in straightening of the Kissinger dependences, as demonstrated in Fig. 6B. Interestingly, the Kissinger dependences exhibit steeper slopes with ↑P2, which would indicate an increase of E, whereas the overall E-T dependence (see Fig. 6A) in fact decreases. This apparent paradox will be further referred to and explained in section 3.1. Correspondingly to the loss of skew, the asymmetry factor AF (see Fig. 6C) decreases with the increase of P2 almost to the values characteristic for the standard non-T-dependent JMA kinetics (AF = 0.53). Even stronger evidence for the acceptable correspondence of the data simulated for ↑P2 with the standard JMA model metrics is the $\alpha_{max,z}$ quantity, which for all data with ↑P2 fall within the extended "standard JMA model" applicability limits: for $r^2 = 0.995$, $\alpha_{max,z} = 0.585 – 0.705$.

2.3. Influence of the absolute A magnitudes in the A-T dependence

The third explored effect was that of changing the pre-exponential factor A, while having the E-T dependence fixed. The two borderline E-T dependences characterized by the

following combinations of the P1&P2 parameters were used: -55&60, -35&25. For each of these dependences, the T-dependent logA was calculated using Eq. 10 with additional optional ΔlogA = 2 or 4 being added to the logA-T dependence (i.e. shifting the whole dependence to higher logA). Similarly to the increase of E (via ↑P2), also the increase of logA leads to a large cease of the JMA peak skewing – see Fig. 7. This result is a consequence of the rate constant K profile not being shifted in temperature but increasing in magnitude – in correspondence with Eq. 1. As such, the crystallization proceeds orders of magnitude faster, leading to the process being finished before the temperatures near the K-T dependence maximum are achieved. The corresponding K-T dependences are again included in the Supplemental online material. Akin situation to the one depicted in Fig. 6B is displayed also for the present series in Fig. 8B. Although the E-T dependences do not change within each series, the Kissinger-derived E clearly increases with the logA value being added in Eq. 10. Detailed explanation will again be provided in section 3.1. Also the AF and $\alpha_{max,z}$ metrics confirm large loss of skew, with all logA-modified simulations providing JMA peaks falling into the $r^2 = 0.995$ category.

2.4. Influence of m_{JMA} kinetic exponent

By far the most interesting and important influence on the skewing of the JMA kinetics is exhibited by the JMA kinetic exponent m_{JMA}. The data simulated for the two borderline tested E-T dependences characterized by the -55&60, -35&25 combinations of the P1&P2 parameters, and for the three typical values of m_{JMA} (1, 2 and 3) are shown in Fig. 9. Note that all the results introduced in the previous sections were always simulated for m_{JMA} = 1. As is apparent, the increasing m_{JMA} manifests differently for both E-T dependences. For the -55&60 combination, the skewing lessens; for the -35&25 combination, the difference in skewing across the q^+ span magnifies. Since the increased JMA kinetic exponents cause the

kinetic peaks to narrow down and (particularly their onsets) to shift to higher T with $\uparrow q^+$, each peak gets to experience more discrete range of the E-T dependence. Accordingly, the kinetics manifesting at different q^+ are based on the significantly different segments of the K-T dependence, which can lead to much larger changes in the kinetic behavior across the probed q^+ range.

For the present simulations, these consequences are quantified in Fig. 10. As results from Fig. 10B, the skewing increases with q^+ (and m_{JMA}) significantly more in the case of the slow decrease of E with T (the process experiences generally larger portion of the K-T dependence, which leads to higher probability of the transformation proceeding over the kinetically critical parts close to the K-T dependence maximum). On the other hand, in the case of the steeper E-T dependence, each narrower (narrowing is caused by $\uparrow m_{JMA}$) kinetic peak experiences only a short segment of K-T, which leads to the decrease of skewing. Correspondingly, for the 55&60 combination, the AF and $\alpha_{max,z}$ metrics get closer to the standard JMA kinetics (with no E(T) implemented) with increasing m_{JMA}, and for the -35&25 combination, the opposite happens. The latter case is particularly important because it very well imitates the real-life scenarios, where for low q^+, the process corresponds to the standard JMA asymmetry and metrics, whereas at high q^+, the asymmetry of the kinetic peak drastically shifts to more positive values, and the empirical Šesták-Berggren model needs to be used to describe the kinetics. As the present research shows, such scenario can be an evidence for the T-dependent activation energy of the crystallization process. Moreover, a combination of the kinetic parameters (E, A, m_{JMA}) and their temperature dependences could be found, for which the shift to the positive asymmetry could occur already at low q^+. In such case, the need for the empirical and semi-empirical models could cease, and practically all crystallization processes would theoretically follow the physically meaningful JMA kinetics.

3. Discussion

In the first part of section 3, the possibilities regarding the actual determination of the E-T dependence by the methods of the nowadays kinetic analysis (as introduced e.g. in [50]) will be briefly discussed. In the second part, the findings and consequences introduced in section 2 will generalized for technically all types of materials by exploring the behavior in the temperature ranges typical for e.g. special non-oxide glasses or polymers.

3.1. Determination of the true E-T dependence

In order to explore the possibilities for the determination of a true E-T dependence from a common set of non-isothermal measurements, the most diverse and representative sets of simulations were selected and evaluated by means of the nowadays standard methodological apparatus of the kinetic analysis. In particular, the Kissinger dependences (Eq. 7) were fitted by the second-order polynomial, and $E_{Kissinger}$ was calculated from the first derivation of the polynomial equation. In addition, the isoconversional methods [47] (one differential and one integral) were used to determine the corresponding dependences of activation energies ($E_{differential}$ and $E_{integral}$) on the degree of conversion α for the simulated data. Note that, as was shown in [51], the choice of a particular isoconversional methodology within each group (integral or differential) is largely irrelevant for the practical purposes, when the potential process complexity is significant. On the other hand, the simultaneous evaluation of both types of isoconversional data can be in certain cases extremely beneficial for revealing the true value of E. [52] The present isocoonversional methods were, however, used without the temperature dependence being implemented, demonstrating mainly the oversimplification arising from the classical averaging approach of these methods.

In Fig. 11, the true E (input into the simulations), $E_{Kissinger}(T)$, the α dependences of $E_{differential}$ and $E_{integral}$, and the $d\alpha \cdot dt^{-1}$ signals simulated for the 0.5 and 20 $°C \cdot min^{-1}$ are shown

for the following P1&P2&m_{JMA} combinations: -55&60&1, -55&60&3, -45&43&1, -45&43&3, -35&25&1, -35&25&3. In none of the cases, either the temperature-dependent Kissinger evaluation or the temperature-independent isoconversional methods provided acceptable estimates of the true E (input into the simulations). It is very important to note that the classical application of the temperature-independent isoconversional methods has for the narrower kinetic processes (generally those with higher m_{JMA}) proposed practically constant E values, which is of course a serious failure of the recognition of the temperature-dependent kinetics. On the other hand, the temperature-dependent evaluation (in our case based on the Kissinger method) correctly identifies (qualitatively) the large change of the kinetics with changing T.

In the previous paragraph, the narrative was purposefully changed from T-dependent E to the T-dependent kinetics being the reason behind the data-distortions leading to the large changes in the peak asymmetry. So far, the changes in the kinetic appearance of the peaks were enforced by simultaneous temperature evolution of E and A, where dissimilar rates of E and A decreases resulted in uneven compensation and, consequently, an extreme on the K-T dependence. A similar result can be, however, achieved even for a constant value of input E and only A being changed. In such case (as well as, technically, also in the previous case), the compensation occurs between the terms A and exp(-E/RT), where the exponential term increases either through E decreasing and T increasing (a more rapid change) or just through the T increase (a slower increase of exp(-E/RT)). The archetypal cases belonging into this category are displayed in Fig. 12. At linear decrease or increase of $\log(A/s^{-1})$, a linear Kissinger dependence (as well as the akin dependences evaluated for different α values within the isoconversional methods) is obtained, resulting in a corresponding shift of $E_{Kissinfer}$ vs. true E. If logA changes non-linearly see Fig. 12C), a curved Kissinger dependence is obtained, resulting in a non-constant $E_{Kissinger}$-T value.

Interestingly, the most delicate equilibrium occurs in case of the pure temperature variation of activation energy, i.e. with A being constant and only E being T-dependent. In that case, the compensation must occur within the exponential term, i.e. by the interaction of the linearly increasing T and exponentially increasing E (the mathematical power function was used in the present case). Example of such kinetics is shown in Fig. 13, where the change of the A across the three graphs leads to a shift of the kinetic peaks higher in T, and to the larger overlaps of these peaks with the onset slope of the K-T dependence. As was demonstrated already in section 2, the most significant asymmetry changes within the JMA kinetics occur when the process manifests itself near the maximum of the K-T dependence – as shown in Fig. 13C. Also in the case of the pure temperature variation of activation energy (with A being constant), the non-monotonic K-T dependence leads to a curvature of the Kissinger dependence represented by the decreasing $E_{Kissinger}$-T (compare this to the increasing true E-T).

In conclusion, none of the standard T_p-based or isoconversional methods (or their variants with implemented E-T dependence) can accurately or reliably reveal the true E-T dependence or even the fact, whether the potential distortion of the JMA peak shape is a result of the T-dependent E, A, or both.

3.2. Universality, origin and consequences of the phenomenon

As was shown in the previous sections, the two key conditions for the change of the JMA peak asymmetry are the existence of the extreme on the K-T dependence, and its overlap with (or close vicinity to) the temperature range of the macroscopic crystal growth (process conversion $\alpha > 10$ %). Whereas the simulations were done for the temperatures corresponding to the typical syntheses of ceramics and glass-ceramics, akin conditions can occur in every temperature range. This is demonstrated in Fig. 14, where the processes in graph A can

represent crystallization of polymers or small organic molecules (e.g. pharmaceutical substances), graph B can represent crystal growth in chalcogenide glasses, and graph C could correspond to the formation of the high-temperature ceramics based on SiO_2 or ZrO_2. The simulations depicted in Fig. 14 were performed for $m_{JMA} = 1$, hence covering rather slow crystal growth processes. The same K-T dependence can be also paired with the f(α) function with e.g. $m_{JMA} = 3$, which would manifest as narrow kinetic peaks, apparently covering practically all types of kinetic behavior. However, it has to be born in mind that the shape-distortion of the JMA peaks occurs only near the maximum of the non-monotonous K-T dependence, where the crystallization process is significantly slowed-down, and thus the kinetic peaks get broadened. Therefore, it still remains a question, whether the present T-dependent changes of the JMA kinetics could be successfully applied also for the rapid high-temperature amorphous-to-crystalline transformations (such as e.g. in the $Y_3Al_5O_{12}$ glass [53]).

Regarding the actual occurrence of the phenomena in glassy materials, several example reports of the temperature-dependent activation energy of crystallization can be found in [34 - 40]. Nevertheless, if one looks though the relevant literature, many more signs of the possible E-T occurrence can be found. Whereas the curved Kissinger plots are probably the most frequent indication of such behavior (mainly due to the popularity of this type of depiction), the measurement errors can sometimes mask the possible curvature (if subtle), or the isoconversional methods are used to determine E instead of the T_p-based methods. In such case, one can look for the other accompanying signs of temperature-dependent crystallization kinetics, such as e.g. the monotonously changing JMA kinetic exponent m or E-α dependence. [54] Note, however, that a curved Kissinger dependence can be also produced by sole A-T dependence (without E being T-dependent) – as shown in Fig. 12C.

In order to correctly recognize and fully account for the temperature-dependent E or A in the crystallization processes of amorphous materials, the understanding to the physico-chemical origin of such behavior needs to be improved. While the present findings regarding the implementation of the E-T and A-T dependences into the description of the crystallization behavior are perfectly valid also for the macroscopically complex (multistep) processes (see e.g. [55]), in the author's opinion, these processes do not represent the fundamental source of the temperature-dependent behavior. Instead of attributing the E-T and/or A-T dependences to the formation of the chemically or location-wise (volume vs. surface) distinct crystalline phases (which is the main source of the macroscopic multistep crystallizations), the origin of these dependences should be more probably sought in slow and continuous microscopic changes of the intrinsic nucleation or crystal growth behavior. One such example may be the crystallization of amorphous selenium [56], where a continuous transition occurs between two spherulitic crystal growth regimes, with each exhibiting significantly different E (the observed kinetic behavior very close to what is simulated in the present paper). Akin behavior could be expected also in the case of simultaneous formation of different polymorphic phases in pharmaceutics or polymers. Nonetheless, extensive research and general awareness of this possibility in the solid-state kinetics community will be needed to crack this nut.

Whereas the present findings could (in theory) lead to a cessation of the empirical and semi-empirical kinetic models in the crystallization kinetics, it is far too early to consider such outcomes. Hence, the main implication for the nowadays solid-state kinetic analysis is that one should be very careful with physico-chemical interpretations of the results provided by the model-free as well as model-based methodologies. The "apparent" E, A and m_{JMA} values given by these methods are still perfectly fine for the kinetic predictions (which is the primary purpose of the solid-state kinetic analysis). However, the interpretation of either E or m_{JMA} values should be done carefully as those values do not necessarily have to reflect what is truly

happening (even from the kinetics point of view) in the material, and the true E and m_{JMA} values can be significantly different from what the nowadays standard kinetic analysis gives us.

4. Conclusions

Theoretical simulations were used to implement the temperature-dependent E and A into the solid-state kinetic equation based on the JMA kinetic model, which led to occurrence of a non-monotonous K-T dependence. If the non-isothermal JMA crystallization process occurs near the maximum of this dependence, the shape of the JMA peak can be significantly distorted up to an exhibition of a positive asymmetry (intrinsically, the JMA kinetics exhibits invariant negative asymmetry for constant E and A). Of particular interest are the cases with the JMA kinetic exponent $m_{JMA} \geq 2$, where at low heating rates, the kinetic peaks exhibit typical negative JMA asymmetry, and at higher heating rates, the asymmetry of the kinetic peaks shifts to the significantly positive values. These findings indicate that the JMA kinetics does not have to be restricted only to the kinetic peaks with rather narrowly defined asymmetry [32]. This extension of the applicability of the JMA kinetics is, however, strictly conditioned by the confirmation of the existence of the temperature-dependent E and/or A. Whereas the curvature of the Kissinger dependence appears to be a reliable indicator of the significantly manifested temperature-dependent E and/or A, no method of the standard kinetic analysis was able to reliably and accurately identify the true courses of E-T or A-T from the non-isothermal data. As the present findings can be naturally extended beyond the application of the JMA model, the implementation of the E-T and A-T dependences into the solid-state kinetic equation seems to be a logical next step in the development of the new approaches to the solid-state kinetic analysis.

Acknowledgments

This work has been supported by the grant LM2023037 from the Ministry of Education, Youth and Sports of the Czech Republic.

References

[1] M. Li, C. Dong, Y. Ma, & H. Jiang, "Light-transmitting lithium aluminosilicate glass-ceramics with excellent mechanical properties based on cluster model design", Nanomaterials, vol. 13, no. 3, p. 530, 2023. https://doi.org/10.3390/nano13030530

[2] A. Velea, F. Sava, P. Badica, M. Burdusel, C. Mihai, A. Galcaet al., "New chalcogenide glass-ceramics based on Ge-Zn-Se for IR applications", Materials, vol. 15, no. 14, p. 5002, 2022. https://doi.org/10.3390/ma15145002

[3] K. Fan, Y. Lin, H. Tsao, H. Chen, S. Lee, Y. Chenget al., "In vivo evaluation of the effects of sintering temperature on the optical properties of dental glass-ceramics", Nanomaterials, vol. 12, no. 13, p. 2187, 2022.

[4] M. Korzhik, G. Dosovitskiy, T. Anniyev, M. Vasilyev, & V. Khabashesku, "Nanoscale engineering of inorganic composite scintillation materials", Materials, vol. 14, no. 17, p. 4889, 2021. https://doi.org/10.3390/ma14174889

[5] M. Li, C. Dong, Y. Ma, & H. Jiang, "Light-transmitting lithium aluminosilicate glass-ceramics with excellent mechanical properties based on cluster model design", Nanomaterials, vol. 13, no. 3, p. 530, 2023. https://doi.org/10.3390/nano13030530

[6] L. Zhang, Y. Sun, Y. Jiang, B. Da, J. Du, S. Wanget al., "Transparent fluoride glass-ceramics with phase-selective crystallization for middle ir photonics", Journal of Materials Chemistry C, vol. 10, no. 36, p. 12947-12956, 2022

[7] H. Jin, L. Liu, & Z. Zhang, "Strain engineering of 2D materials: issues and opportunities at the interface", Advanced Materials, vol. 31, no. 45, p. 1805417, 2019. https://doi.org/10.1002/adma.201805417

[8] H. Jiang, Y. Lu, L. Ding, W. Lu, G. Fan, & Y. Shi, "Effects of Y2O3-LaF3 on the low temperature sintering and thermal conductivity of aln ceramics", Microelectronics International, vol. 36, no. 1, p. 22-25, 2019. https://doi.org/10.1108/mi-03-2018-0016

[9] D. Wang, B. Siame, S. Zhang, G. Wang, X. Ju, J. Liet al., "Direct integration of cold sintered, temperature-stable Bi2Mo2O9-K2MoO4 ceramics on printed circuit boards for satellite navigation antennas", Journal of the European Ceramic Society, vol. 40, no. 12, p. 4029-4034, 2020

[10] S. Danewalia and K. Singh, "Bioactive glasses and glass–ceramics for hyperthermia treatment of cancer: state-of-art, challenges, and future perspectives", Materials Today Bio, vol. 10, p. 100100, 2021.

[11] O. Saad, A. Salem, & I. Badr, "Preparation and characterization of high chemical durability and low thermal expansion borosilicate glass-ceramics by recycling of borosilicate glass", Egyptian Journal of Chemistry, vol. 64, no. 0, p. 2193-2199, 2021. https://doi.org/10.21608/ejchem.2021.54579.3139

[12] L. Fu, H. Engqvist, & W. Xia, "Glass–ceramics in dentistry: a review", Materials, vol. 13, no. 5, p. 1049, 2020. https://doi.org/10.3390/ma13051049
[13] L. Maloo, A. Patel, S. Toshniwal, & A. Bagde, "Smart materials leading to restorative dentistry: an overview", Cureus, 2022. https://doi.org/10.7759/cureus.30789
[14] M. Cannio, D. Bellucci, J. Roether, D. Boccaccini, & V. Cannillo, "Bioactive glass applications: a literature review of human clinical trials", Materials, vol. 14, no. 18, p. 5440, 2021. https://doi.org/10.3390/ma14185440
[15] D. Filip, V. Surdu, A. Paduraru, & E. Andronescu, "Current development in biomaterials—hydroxyapatite and bioglass for applications in biomedical field: a review", Journal of Functional Biomaterials, vol. 13, no. 4, p. 248, 2022. https://doi.org/10.3390/jfb13040248
[16] G. Wei, F. Luo, Y. Miao, W. Han, Y. Xie, Z. Xuet al., "Treatment of zeolite adsorbed material as a potential nuclear waste glass-ceramic matrix", Journal of the American Ceramic Society, vol. 105, no. 1, p. 257-267, 2021. https://doi.org/10.1111/jace.18094
[17] D. Gregg, E. Vance, P. Dayal, Z. Aly, R. Holmes, & G. Triani, "Hot isostatically pressed (hiped) fluorite glass-ceramic wasteforms for fluoride molten salt wastes", Journal of the American Ceramic Society, vol. 103, no. 10, p. 5454-5469, 2020. https://doi.org/10.1111/jace.17293
[18] D. Sciti, A. Vinci, L. Zoli, P. Galizia, S. Failla, S. Mungiguerraet al., "Propulsion tests on ultra-high-temperature ceramic matrix composites for reusable rocket nozzles", Journal of Advanced Ceramics, vol. 12, no. 7, p. 1345-1360, 2023. https://doi.org/10.26599/jac.2023.9220759
[19] S. Singh and A. Sontakke, "Transparent glass ceramics", Crystals, vol. 11, no. 2, p. 156, 2021. https://doi.org/10.3390/cryst11020156
[20] N. Mahyon, T. Li, R. Martinez-Botas, Y. Li, & K. Li, "A new hollow fibre catalytic converter design for sustainable automotive emissions control", Catalysis Communications, vol. 120, p. 86-90, 2019. https://doi.org/10.1016/j.catcom.2018.12.001
[21] S. Hajimirzaee, D. Shaw, P. Howard, & A. Doyle, "Industrial scale 3D printed catalytic converter for emissions control in a dual-fuel heavy-duty engine", Chemical Engineering Science, vol. 231, p. 116287, 2021. https://doi.org/10.1016/j.ces.2020.116287
[22] J. Šesták. Thermophysical Properties of Solids, Their Measurements and Theoretical Analysis. Elsevier: Amsterdam, 1984.
[23] S. Karthika, T. Radhakrishnan, & P. Kalaichelvi, "A review of classical and nonclassical nucleation theories", Crystal Growth & Design, vol. 16, no. 11, p. 6663-6681, 2016. https://doi.org/10.1021/acs.cgd.6b00794
[24] C. Zhu, "Nucleation and crystallization of polymer melts under cyclic stretching: entanglement effect", Macromolecules, vol. 56, no. 14, p. 5490-5501, 2023. https://doi.org/10.1021/acs.macromol.3c00461
[25] S. Xu, Z. Hou, X. Chuai, & Y. Wang, "Overview of secondary nucleation: from fundamentals to application", Industrial & Engineering Chemistry Research, vol. 59, no. 41, p. 18335-18356, 2020. https://doi.org/10.1021/acs.iecr.0c03304
[26] W.A. Johnson, K.F. Mehl. Reaction kinetics in processes of nucleation and growth. Trans. Am. Inst. Min. (Metall) Eng. 135 (1939) 416–42.
[27] M. Avrami. Kinetics of phase change I–general theory. J. Chem. Phys. 7 (1939) 1103–12.
[28] M. Avrami. Kinetics of phase change. II–transformation-time relations for random distribution of nuclei. J. Chem. Phys. 7 (1940) 212–24.

[29] M. Avrami. Granulation, phase change, and microstructure – kinetics of phase change III. J. Chem. Phys. 7 (1941) 177–84.
[30] A.N. Kolmogorov. On the statistical theory of the crystallization of metals. Bull. Acad. Sci. USSR 1 (1937) 355–359
[31] J. Šesták. Science of Heat and Thermophysical Studies: A Generalized Approach to Thermal Analysis, Elsevier, Amsterdam, 2005.
[32] R. Svoboda. Crystallization of glasses – When to use the Johnson-Mehl-Avrami kinetics? J. Eur. Ceram. Soc. 41 (2021) 7862 – 7867
[33] R. Svoboda. Usage of masterplots in kinetic analysis of complex surface/volume crystallization processes in Se-Te glasses. J. Non-Cryst. Sol. 541 (2020) 120068.
[34] B. Chen, D. Wal, G. Brink, G. Palasantzas, & B. Kooi, "Resolving crystallization kinetics of GeTe phase-change nanoparticles by ultrafast calorimetry", Crystal Growth & Design, vol. 18, no. 2, p. 1041-1046, 2017. https://doi.org/10.1021/acs.cgd.7b01498
[35] H. Weber, J. Orava, I. Kaban, J. Pries, & A. Greer, "Correlating ultrafast calorimetry, viscosity, and structural measurements in liquid gete and Ge15Te85", Physical Review Materials, vol. 2, no. 9, 2018. https://doi.org/10.1103/physrevmaterials.2.093405
[36] J. Kohout, "Modified arrhenius equation in materials science, chemistry and biology", Molecules, vol. 26, no. 23, p. 7162, 2021. https://doi.org/10.3390/molecules26237162
[37] El-Oyoun, M.A. Evaluation of the transformation kinetics of Ga7.5Se92.5 chalcogenide glass using the theoretical method developed and isoconversional analyses. J. Alloys Compd. 2010, 507, 6–15.
[38] Luo, X.; Han, L.; Gu, J. Study on Austenitization Kinetics of SA508 Gr.3 Steel Based on Isoconversional Method. Metals 2016, 6, 8.
[39] Holba, P.; Šesták, J. Imperfections of Kissinger Evaluation Method and Crystallization Kinetics. Glass Phys. Chem. 2014, 40, 486–495
[40] Zhou, Z.N.; Yang, L.; Li, R.C.; Li, J.; Hu, Q.D.; Li, J.G. Martensitic transformations and kinetics in Ni-Mn-In-Mg shape memory alloys. Intermetallics 2018, 92, 49–54.
[41] R. Svoboda, J. Chovanec, S. Slang, L. Beneš, P. Konrád. Single-curve multivariate kinetic analysis: Application to the crystallization of commercial Fe-Si-Cr-B amorphous alloys. J. Alloys Compd. 889 (2022) 161672
[42] M. Chromčíková, R. Svoboda, B. Hruška, B. Pecušová, A. Nowicka. Thermo-kinetic and structural characterization of Ce-doped glasses based on Bioglass 45S5. Materials Chemistry and Physics 304 (2023) 127833. https://doi.org/10.1016/j.matchemphys.2023.127833
[43] M.H. Cohen, D. Turnbull. Molecular Transport in Liquids and Glasses. J. Chem. Phys. 31 (1959) 1164-1169
[44] Jackson, K.A. (1975). Theory of Crystal Growth. In: Hannay, N.B. (eds) Changes of State. Treatise on Solid State Chemistry, vol 5. Springer, Boston, MA. https://doi.org/10.1007/978-1-4757-1120-2_5
[45] Orava, J., Greer, A., Gholipour, B. et al. Characterization of supercooled liquid $Ge_2Sb_2Te_5$ and its crystallization by ultrafast-heating calorimetry. Nature Mater 11, 279–283 (2012). https://doi.org/10.1038/nmat3275
[46] Orava, J., Hewak, D.W. and Greer, A.L. (2015), Fragile-to-Strong Crossover in Supercooled Liquid Ag-In-Sb-Te Studied by Ultrafast Calorimetry. Adv. Funct. Mater., 25: 4851-4858
[47] Vyazovkin, S.; Burnham, A.K.; Favergeon, L.; Koga, N.; Moukhina, E.; Pérez-Maqueda, L.A.; Sbirrazzuoli, N. ICTAC Kinetics Committee recommendations for analysis of multi-step kinetics. Thermochim. Acta 2020, 689, 178597. https://doi.org/10.1016/j.tca.2020.178597

[48] Kissinger, H.E. Reaction Kinetics in Differential Thermal Analysis. Anal. Chem. 1957, 29, 1702–1706. https://doi.org/10.1021/ac60131a045
[49] P.J. Barrie. The mathematical origins of the kinetic compensation effect: 1. the effect of random experimental errors. Phys. Chem. Chem. Phys., 2012,14, 318-326.
[50] D. Brandová, R. Svoboda, Z. Olmrová Zmrhalová, J. Chovanec, R. Bulánek. Crystallization kinetics of glassy materials: the ultimate complexity? J. Therm. Anal. Calorim. 134 (2018) 825-834
[51] G. Luciano, R. Svoboda. Activation energy determination in case of independent complex kinetic processes. Processes 7 (2019) 738
[52] R. Svoboda, G. Luciano. Complex proces activation energy evaluated by combined utilization of differential and integral isoconversional methods. J. Non-Cryst. Sol. 535 (2020) 120003
[53] J. Chovanec, R. Svoboda, J. Kraxner, A. Černá, D. Galusek. Crystallization kinetics of the $Y_3Al_5O_{12}$. J. Alloys, Compd. 725 (2017) 792 – 799
[54] G.V.P. Bezerra, L.S. Everton, A.M.C. Costa, A. Rojas, A.M. Rodrigues, A.A. Cabral, Crystallization kinetics in a lithium disilicate glass revisited: Model-free and model-fitting approaches. J. Non-Cryst. Sol. 617 (2023) 122494.
[55] J. Kaur, N.K. Mattu, I. Mudahar, K. Singh. Role of Sm2O3 on surface to bulk crystallization and thermal properties of Fe2O3-V2O5-B2O3-SiO2 glasses. J. Non-Cryst. Sol. 610 (2023) 122304.
[56] J. Málek, R. Svoboda. Kinetic processes in amorphous materials revealed by thermal analysis: Application to glassy selenium. Molecules 24 (2019) 2725.

Figure captions

Fig. 1: A) Visualization of the borderline JMA asymmetries (black and red lines) set according [32], and the maximum asymmetries of kinetic peaks encountered experimentally.
B) Demonstration of the determination of $\alpha_{max,z}$ (red line, top and right axes; Eq. 4), and AF and TF (black line, bottom and left axes; Eqs. 5 and 6).

Fig. 2: A) Example of a set of JMA kinetic peaks simulated for 7 different heating rates and Eq. 1 with constant E and A.
B) Example of a set of JMA kinetic peaks simulated for 7 different heating rates and Eq. 1 with temperature-dependent E and A.
C) Temperature dependences of E, A and K for the JMA data depicted in graph A.
D) Temperature dependences of E, A and K for the JMA data depicted in graph B.

Fig. 3: A) – E) Examples of the series of JMA peaks simulated for the 7 listed heating rates, and E(T) and A(T) dependences expressed by Eqs. 9 and 10. The parameters P1 and P2 from Eq. 9 are listed in each respective graph.
F) E(T) dependences expressed by Eq. 9 for the different combinations of P1 and P2 parameters.

Fig. 4: A) Kissinger dependences based on the data from Figs. 3A – 3E (points) fit by the second-order polynomials (lines).
B) – D) AF, TF and $\alpha_{max,z}$ values determined for the data from Figs. 3A – 3E.

Fig. 5: A) – F) Examples of the series of JMA peaks simulated for the 7 listed heating rates, and E(T) and A(T) dependences expressed by Eqs. 9 and 10. The parameters P1 and P2 from Eq. 9 are listed in each respective graph.

Fig. 6: A) E(T) dependences expressed by Eq. 9 for the different combinations of P1 and P2 parameters from Fig. 5.
B) Kissinger dependences based on the data from Figs. 5A – 5F (points) fit by the second-order polynomials (lines).
C) – D) AF and $\alpha_{max,z}$ values determined for the data from Figs. 5A – 5F.

Fig. 7: A) – F) Examples of the series of JMA peaks simulated for the 7 listed heating rates, and E(T) and A(T) dependences expressed by Eqs. 9 and 10. The parameters P1 and P2 from Eq. 9 are listed in each respective graph. In addition, the ΔlogA values added to the A(T) dependence expressed by Eqs. 10 are shown in each graph.

Fig. 8: A) E(T) dependences expressed by Eq. 9 for the different combinations of P1 and P2 parameters from Fig. 7.
B) Kissinger dependences based on the data from Figs. 7A – 7F (points) fit by the second-order polynomials (lines).
C) – D) AF and $\alpha_{max,z}$ values determined for the data from Figs. 7A – 7F.

Fig. 9: A) – F) Examples of the series of JMA peaks simulated for the 7 listed heating rates, and E(T) and A(T) dependences expressed by Eqs. 9 and 10. The parameters P1 and P2 from Eq. 9 are listed in each respective graph. In addition, the m_{JMA} values are shown in each graph.

Fig. 10: A) E(T) dependences expressed by Eq. 9 for the different combinations of P1 and P2 parameters from Fig. 9.
B) Kissinger dependences based on the data from Figs. 9A – 9F (points) fit by the second-order polynomials (lines).
C) – D) AF and $\alpha_{max,z}$ values determined for the data from Figs. 9A – 9F.

Fig. 11: Comparison of the data evaluated for the series of JMA peaks simulated for different combinations of parameters P1, P2 and m_{JMA}. The solid lines (bottom and left axes) correspond to the true E values (input into the simulations) and the E values determined by the derivation of the Kissinger dependences. The dashed lines (bottom and right axes) show the JMA peaks simulated at 0.5 and 20 °C·min^{-1}. Points (top and left axes) show the E values determined by the isoconversional methods in dependence on the degree of conversion α. For these data, both E and A are non-constant.

Fig. 12: Comparison of the data evaluated for the series of JMA peaks simulated for different logA(T) dependences; true E values were 500 kJ·mol^{-1}, and m_{JMA} = 1. The colored solid lines (bottom and left axes) correspond to the true E values (input into the simulations) and the E values determined by the derivation of the Kissinger dependences. The black solid lines (bottom and second left axes) correspond to the temperature dependences of logA. The dashed lines (bottom and right axes) show the JMA peaks simulated at 0.5 and 20 °C·min^{-1}. Points (top and left axes) show the E values determined by the isoconversional methods in dependence on the degree of conversion α. For these data, E is constant and A is non-constant.

Fig. 13: Comparison of the data evaluated for the series of JMA peaks simulated for different E(T) dependences; logA values were constant, and $m_{JMA} = 3$. The colored solid lines (bottom and left axes) correspond to the true E values (input into the simulations) and the E values determined by the derivation of the Kissinger dependences. The black solid lines (bottom and second left axes) correspond to the temperature dependences of the rate constant K. The dashed lines (bottom and right axes) show the JMA peaks simulated at 0.5 and 20 $°C \cdot min^{-1}$. Points (top and left axes) show the E values determined by the isoconversional methods in dependence on the degree of conversion α. For these data, E is non-constant and A is constant.

Fig. 14: Demonstration of the qualitative similarity of the JMA peaks asymmetry change for different temperature regions. The colored solid lines (bottom and both left axes) correspond to the true E and A values (input into the simulations). The black solid lines (bottom and right axes) correspond to the temperature dependences of the rate constant K. The dashed lines (bottom and right axes) show the JMA peaks simulated at 0.5 and 20 $°C \cdot min^{-1}$. For these data, both E and A are non-constant.

Fig. 1

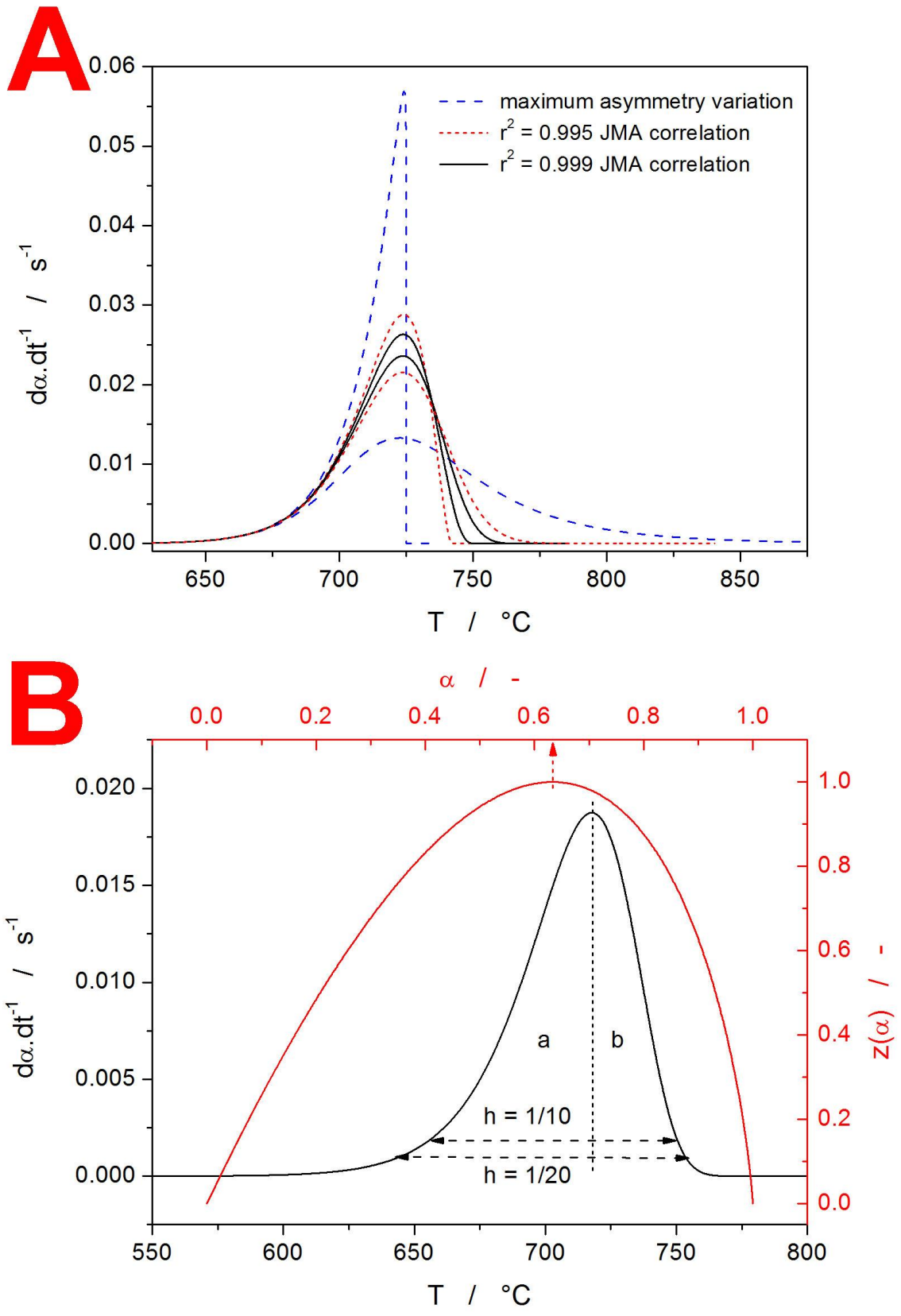
A
maximum asymmetry variation
r² = 0.995 JMA correlation
r² = 0.999 JMA correlation
dα.dt⁻¹ / s⁻¹
T / °C
B
α / -
dα.dt⁻¹ / s⁻¹
z(α) / -
a
b
h = 1/10
h = 1/20
T / °C

Fig. 2

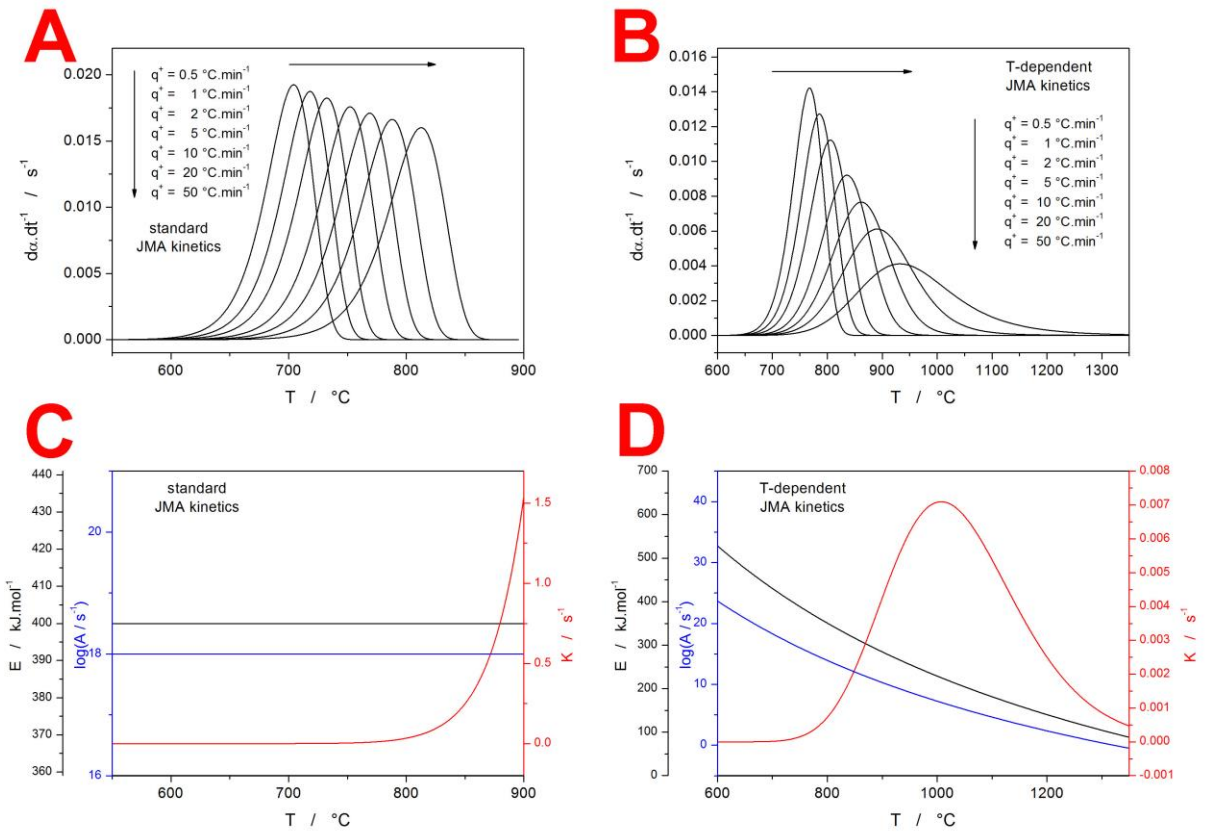
A
B
C
D
standard
JMA kinetics
T-dependent
JMA kinetics
T / °C
dα.dt-1 / s-1
E / kJ.mol-1
log(A / s-1)
K / s-1

Fig. 3

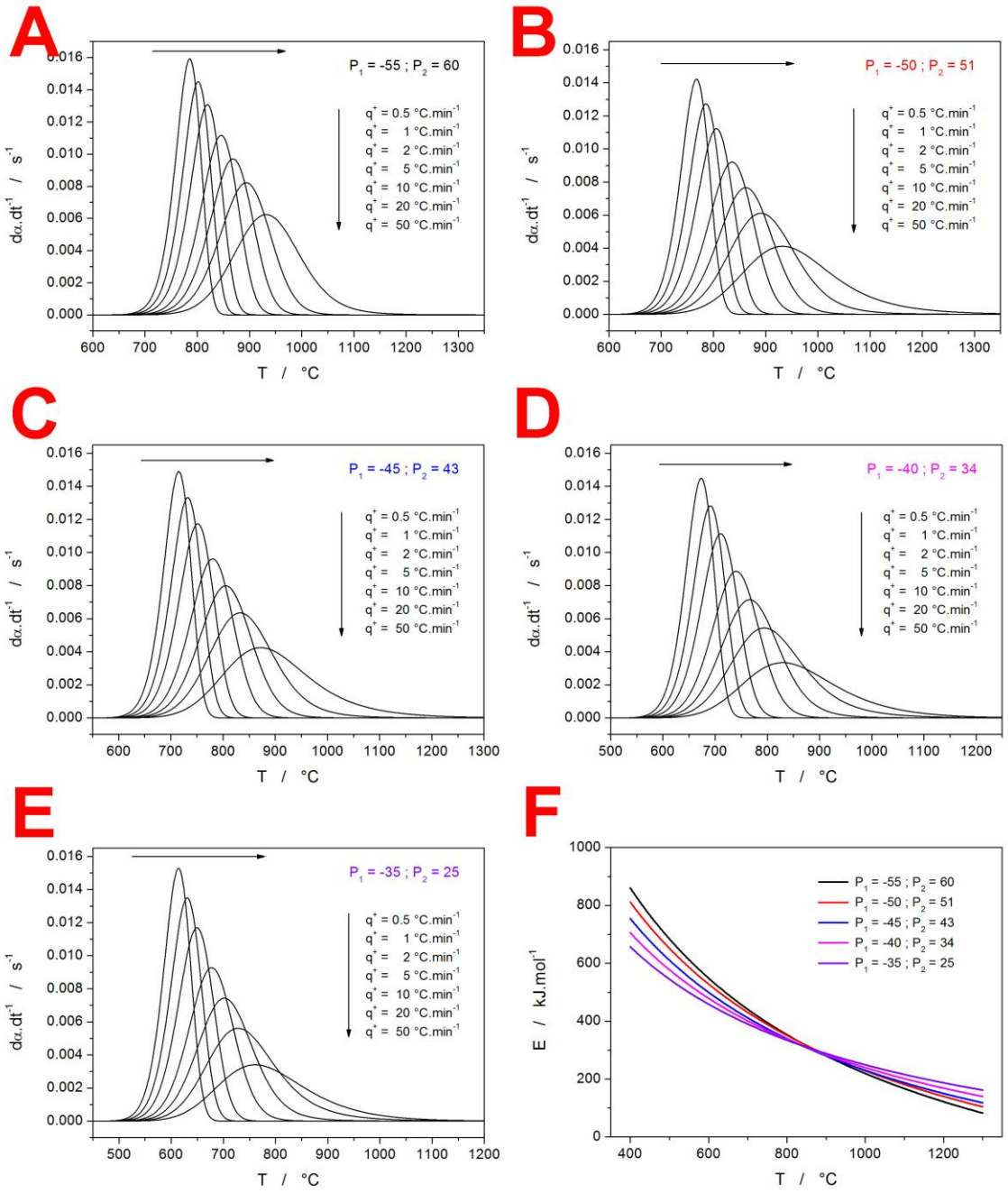
A
B
C
D
E
F
dα.dt-1 / s-1
T / °C
E / kJ.mol-1
P1 = -55 ; P2 = 60
P1 = -50 ; P2 = 51
P1 = -45 ; P2 = 43
P1 = -40 ; P2 = 34
P1 = -35 ; P2 = 25
q+ = 0.5 °C.min-1
q+ = 1 °C.min-1
q+ = 2 °C.min-1
q+ = 5 °C.min-1
q+ = 10 °C.min-1
q+ = 20 °C.min-1
q+ = 50 °C.min-1

Fig. 4

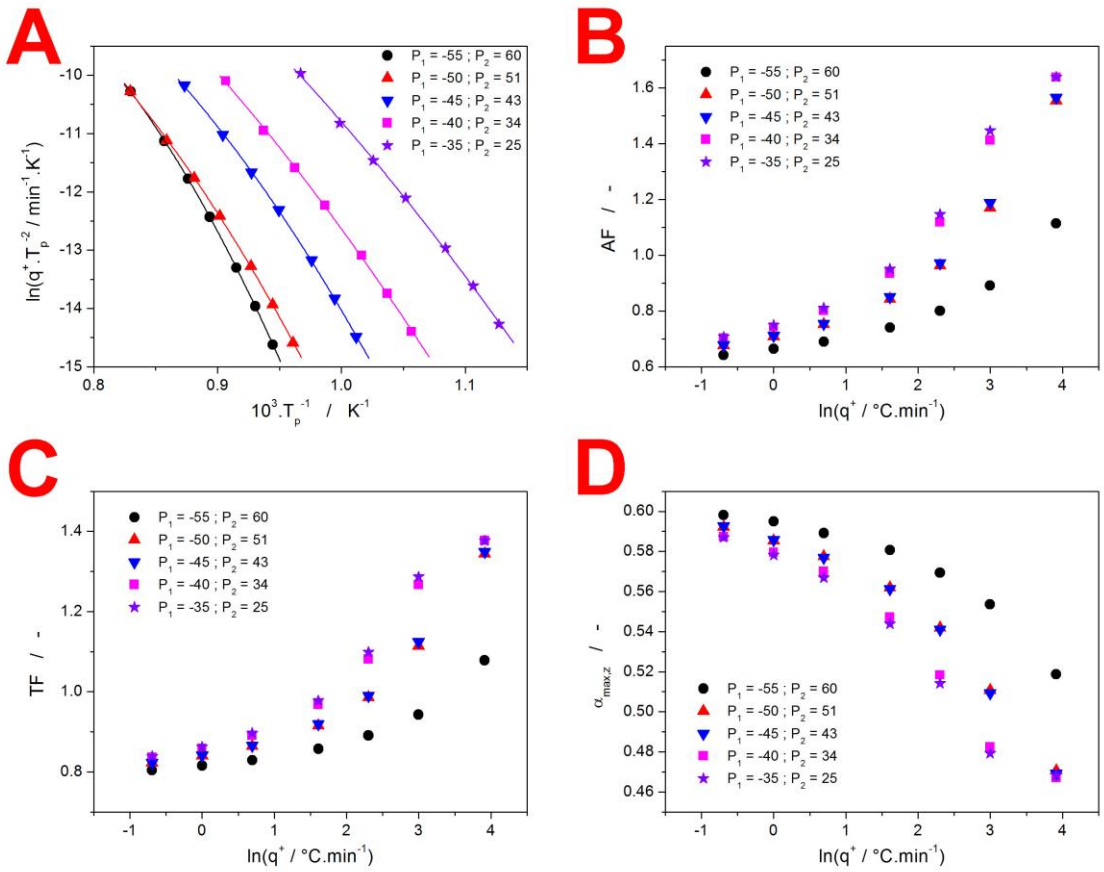
A
B
C
D
P1 = -55 ; P2 = 60
P1 = -50 ; P2 = 51
P1 = -45 ; P2 = 43
P1 = -40 ; P2 = 34
P1 = -35 ; P2 = 25
ln(q+.Tp-2 / min-1.K-1)
10^3.Tp-1 / K-1
AF / -
ln(q+ / °C.min-1)
TF / -
αmax,z / -

Fig. 5

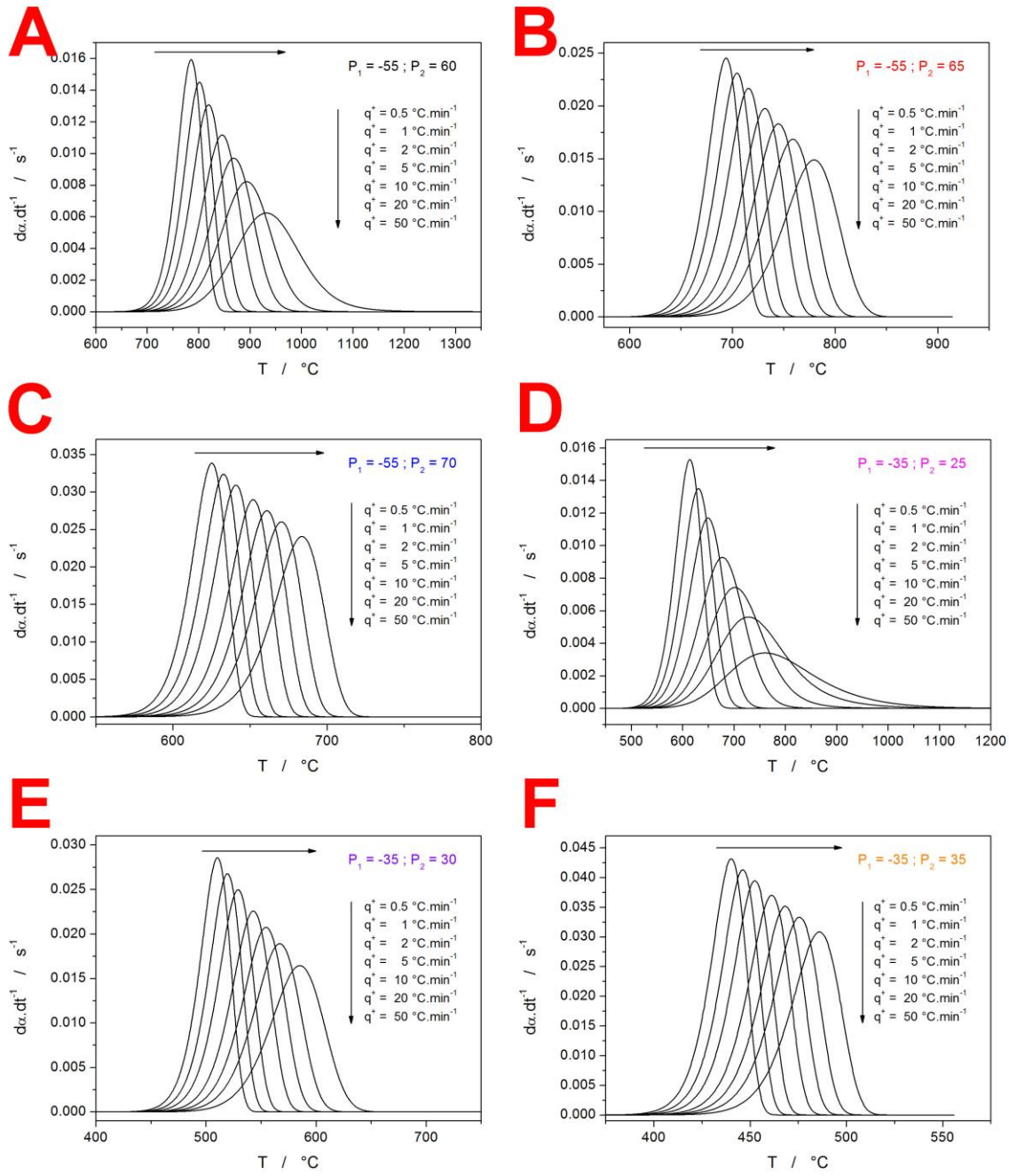
A
P1 = -55 ; P2 = 60
B
P1 = -55 ; P2 = 65
C
P1 = -55 ; P2 = 70
D
P1 = -35 ; P2 = 25
E
P1 = -35 ; P2 = 30
F
P1 = -35 ; P2 = 35
q+ = 0.5 °C.min-1
q+ = 1 °C.min-1
q+ = 2 °C.min-1
q+ = 5 °C.min-1
q+ = 10 °C.min-1
q+ = 20 °C.min-1
q+ = 50 °C.min-1
dα.dt-1 / s-1
T / °C

Fig. 6

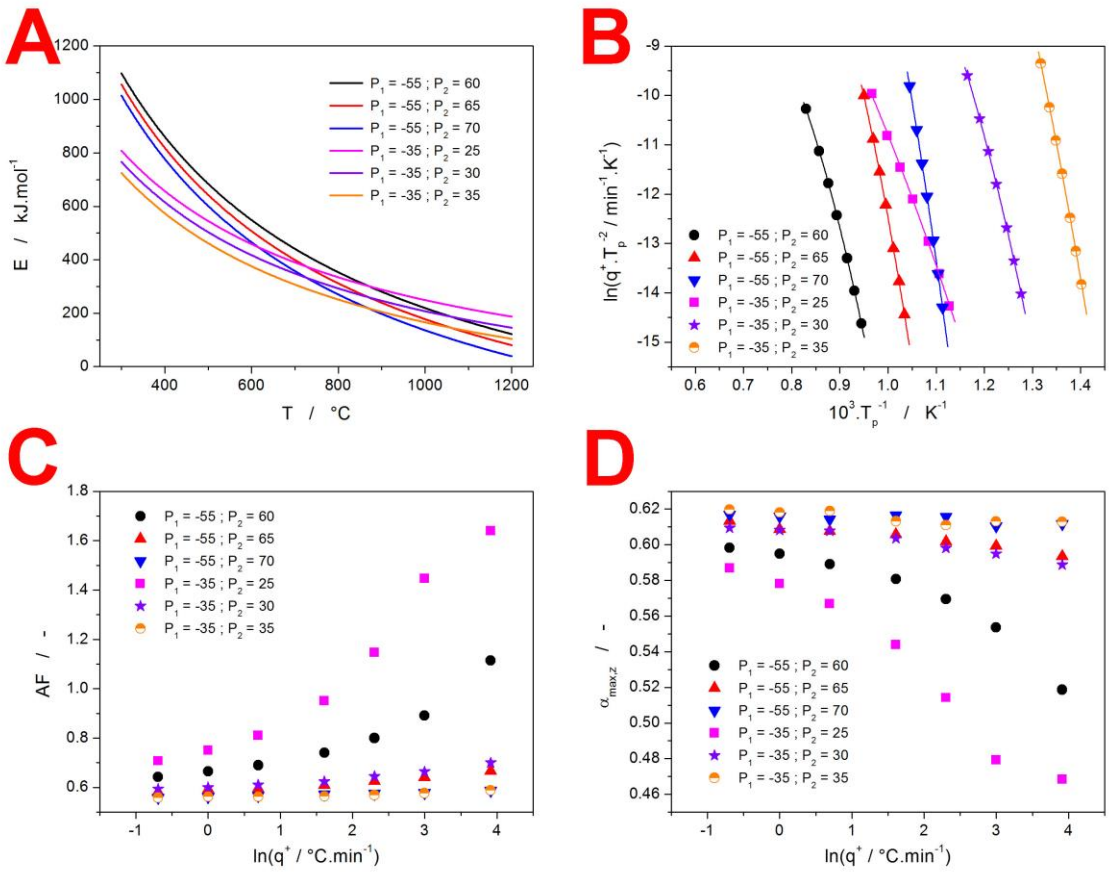
A
E / kJ.mol-1
T / °C
P1 = -55 ; P2 = 60
P1 = -55 ; P2 = 65
P1 = -55 ; P2 = 70
P1 = -35 ; P2 = 25
P1 = -35 ; P2 = 30
P1 = -35 ; P2 = 35
B
ln(q+.Tp-2 / min-1.K-1)
10³.Tp-1 / K-1
C
AF / -
ln(q+ / °C.min-1)
D
αmax,z / -
ln(q+ / °C.min-1)

Fig. 7

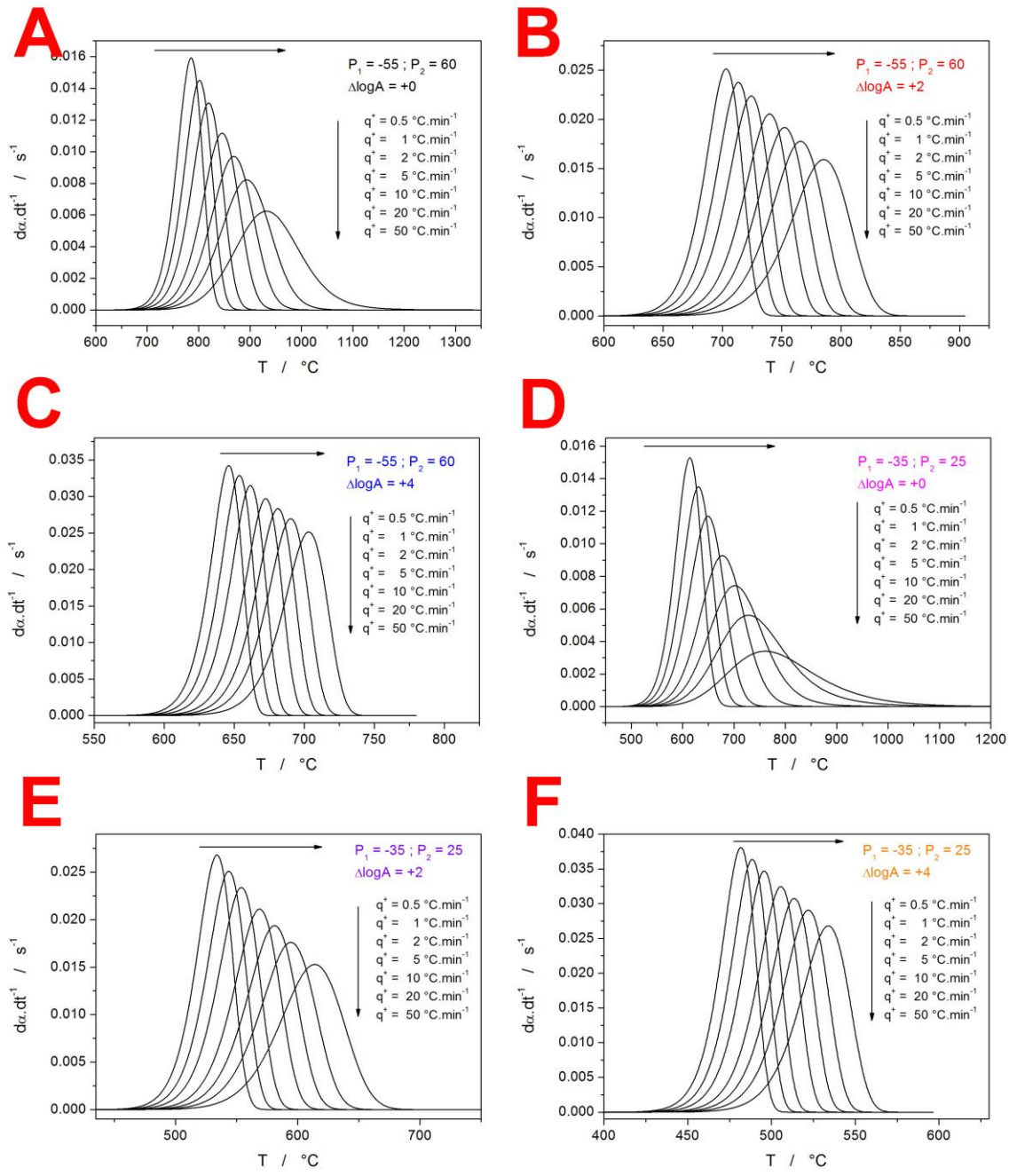
A
P1 = -55 ; P2 = 60
ΔlogA = +0
q+ = 0.5 °C.min-1
q+ = 1 °C.min-1
q+ = 2 °C.min-1
q+ = 5 °C.min-1
q+ = 10 °C.min-1
q+ = 20 °C.min-1
q+ = 50 °C.min-1
dα.dt-1 / s-1
T / °C
B
P1 = -55 ; P2 = 60
ΔlogA = +2
C
P1 = -55 ; P2 = 60
ΔlogA = +4
D
P1 = -35 ; P2 = 25
ΔlogA = +0
E
P1 = -35 ; P2 = 25
ΔlogA = +2
F
P1 = -35 ; P2 = 25
ΔlogA = +4

Fig. 8

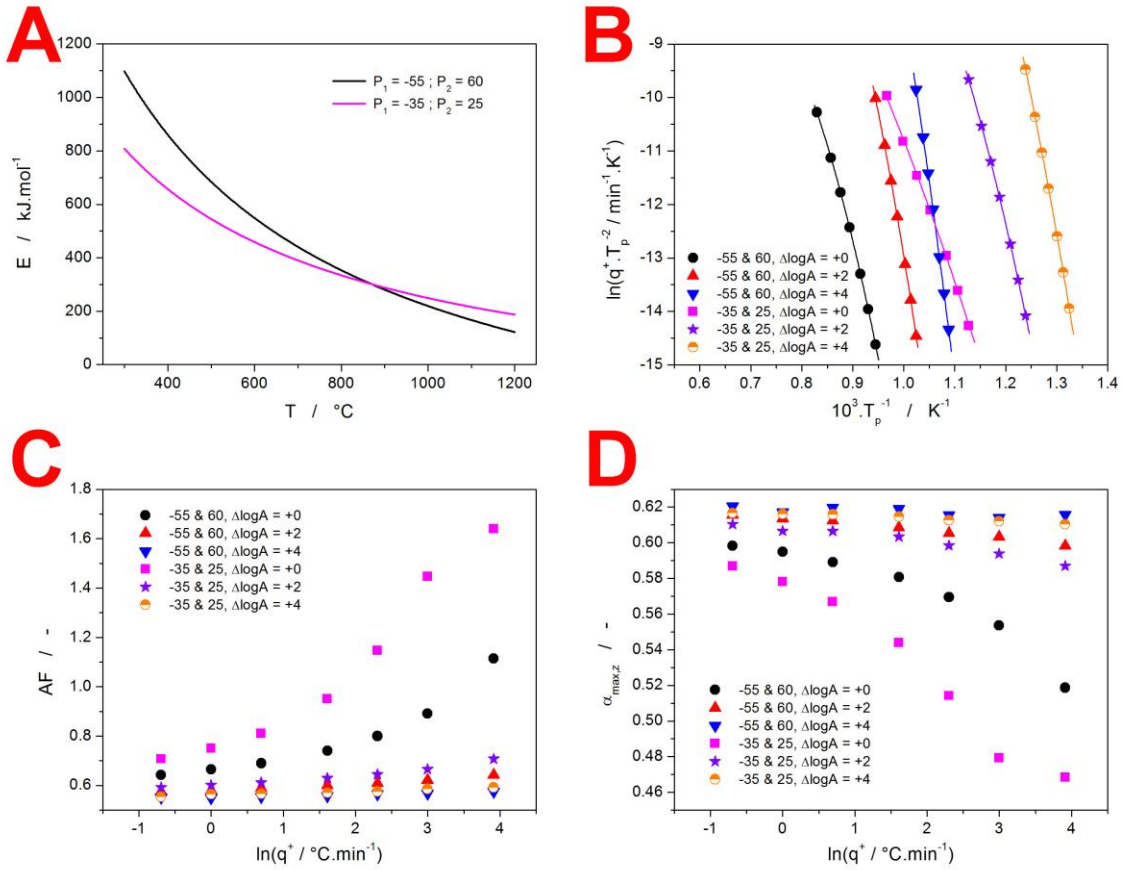
A
E / kJ.mol-1
T / °C
P1 = -55 ; P2 = 60
P1 = -35 ; P2 = 25
B
ln(q+.Tp-2 / min-1.K-1)
10^3.Tp-1 / K-1
-55 & 60, ΔlogA = +0
-55 & 60, ΔlogA = +2
-55 & 60, ΔlogA = +4
-35 & 25, ΔlogA = +0
-35 & 25, ΔlogA = +2
-35 & 25, ΔlogA = +4
C
AF / -
ln(q+ / °C.min-1)
D
αmax,z / -
ln(q+ / °C.min-1)

Fig. 9

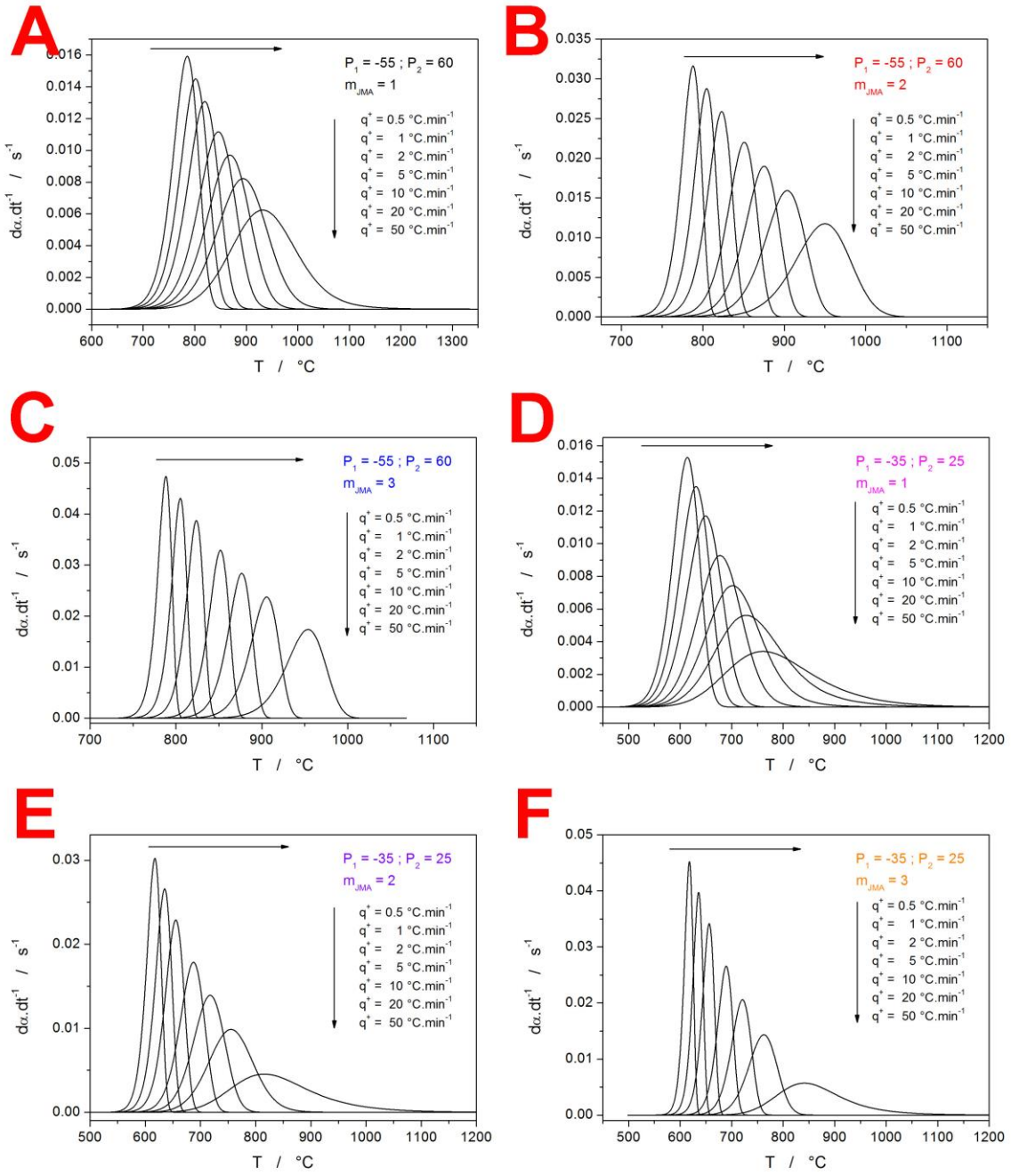
A
P1 = -55 ; P2 = 60
mJMA = 1
B
P1 = -55 ; P2 = 60
mJMA = 2
C
P1 = -55 ; P2 = 60
mJMA = 3
D
P1 = -35 ; P2 = 25
mJMA = 1
E
P1 = -35 ; P2 = 25
mJMA = 2
F
P1 = -35 ; P2 = 25
mJMA = 3
q+ = 0.5 °C.min-1
q+ = 1 °C.min-1
q+ = 2 °C.min-1
q+ = 5 °C.min-1
q+ = 10 °C.min-1
q+ = 20 °C.min-1
q+ = 50 °C.min-1
dα.dt-1 / s-1
T / °C

Fig. 10

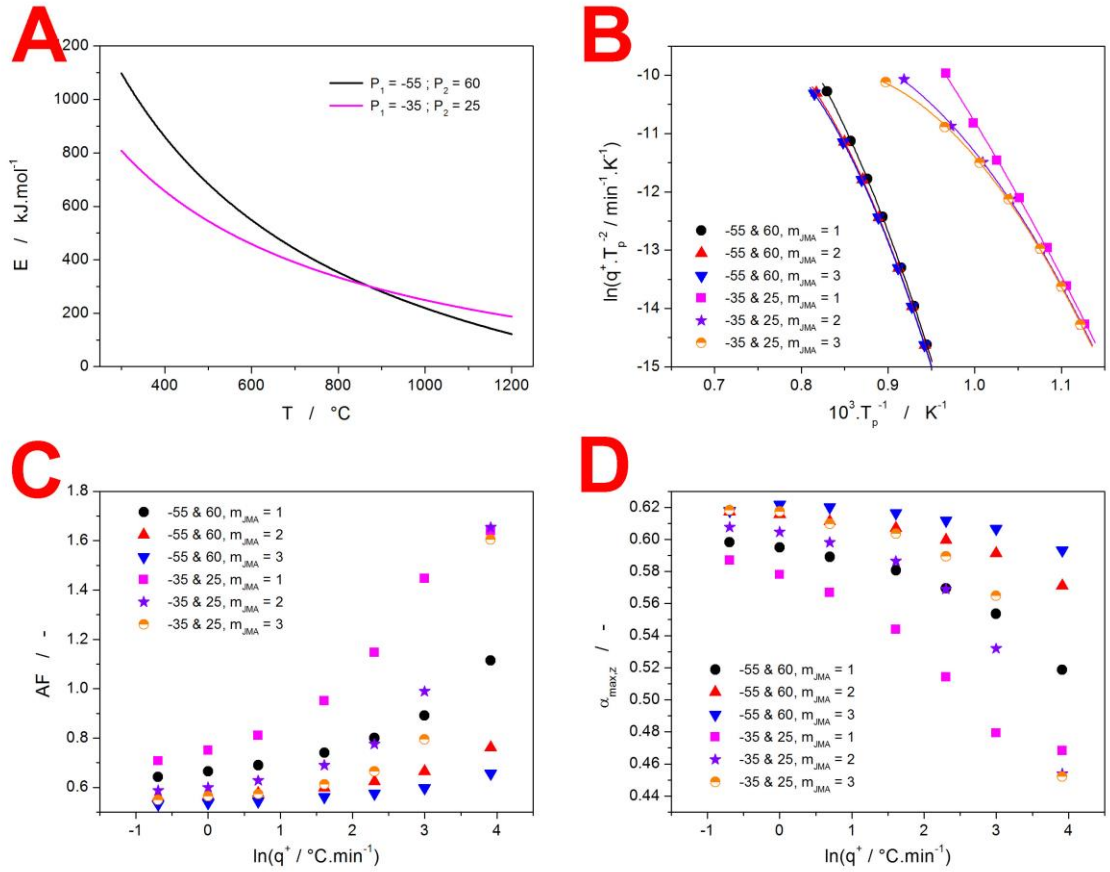
A
E / kJ.mol-1
T / °C
P1 = -55 ; P2 = 60
P1 = -35 ; P2 = 25
B
ln(q+.Tp-2 / min-1.K-1)
10³.Tp-1 / K-1
-55 & 60, mJMA = 1
-55 & 60, mJMA = 2
-55 & 60, mJMA = 3
-35 & 25, mJMA = 1
-35 & 25, mJMA = 2
-35 & 25, mJMA = 3
C
AF / -
ln(q+ / °C.min-1)
D
αmax,z / -
ln(q+ / °C.min-1)

Fig. 11

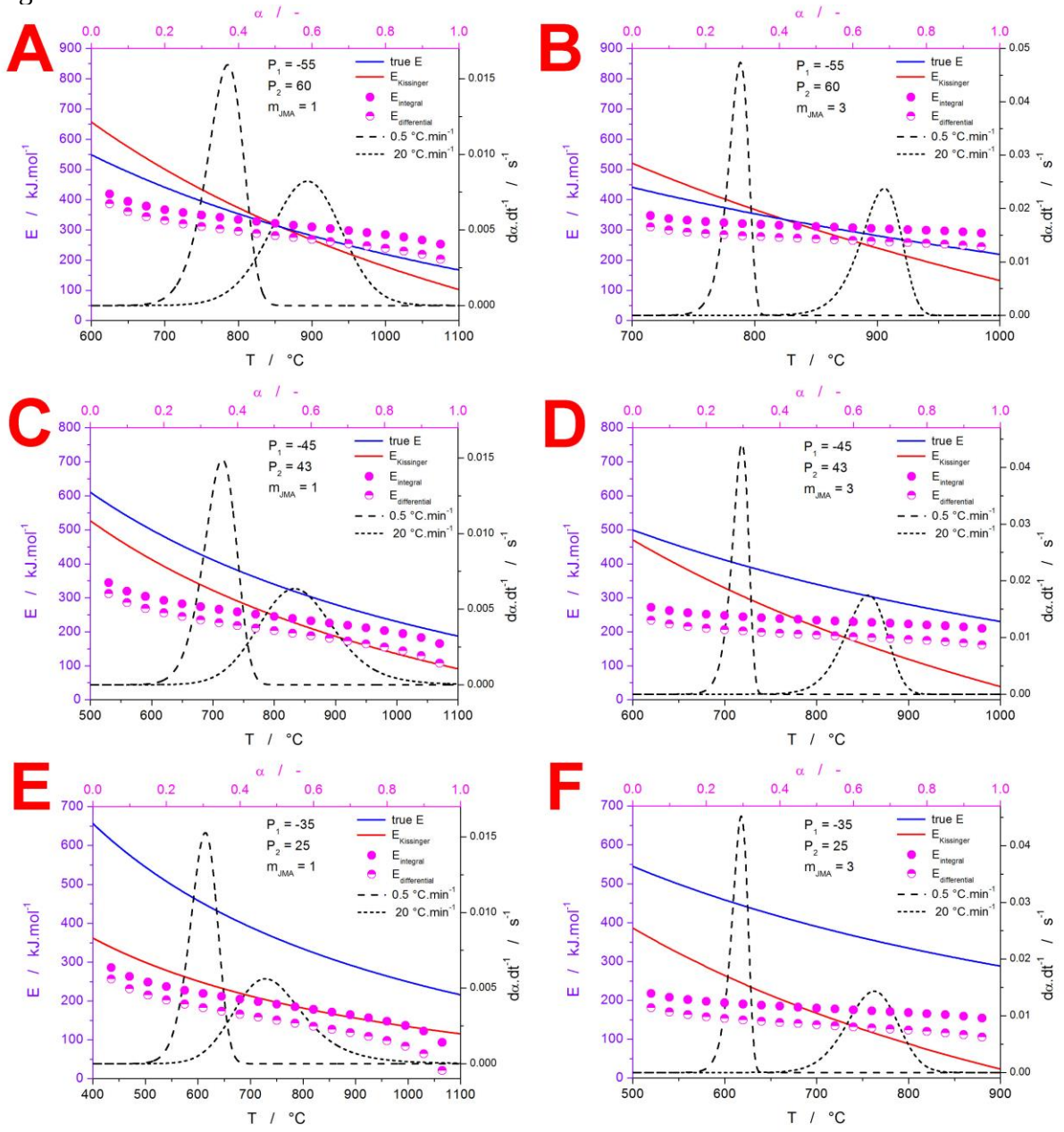
A
B
C
D
E
F
α / -
E / kJ.mol-1
dα.dt-1 / s-1
T / °C
true E
EKissinger
Eintegral
Edifferential
0.5 °C.min-1
20 °C.min-1
P1 = -55
P2 = 60
mJMA = 1
P1 = -55
P2 = 60
mJMA = 3
P1 = -45
P2 = 43
mJMA = 1
P1 = -45
P2 = 43
mJMA = 3
P1 = -35
P2 = 25
mJMA = 1
P1 = -35
P2 = 25
mJMA = 3

Fig. 12

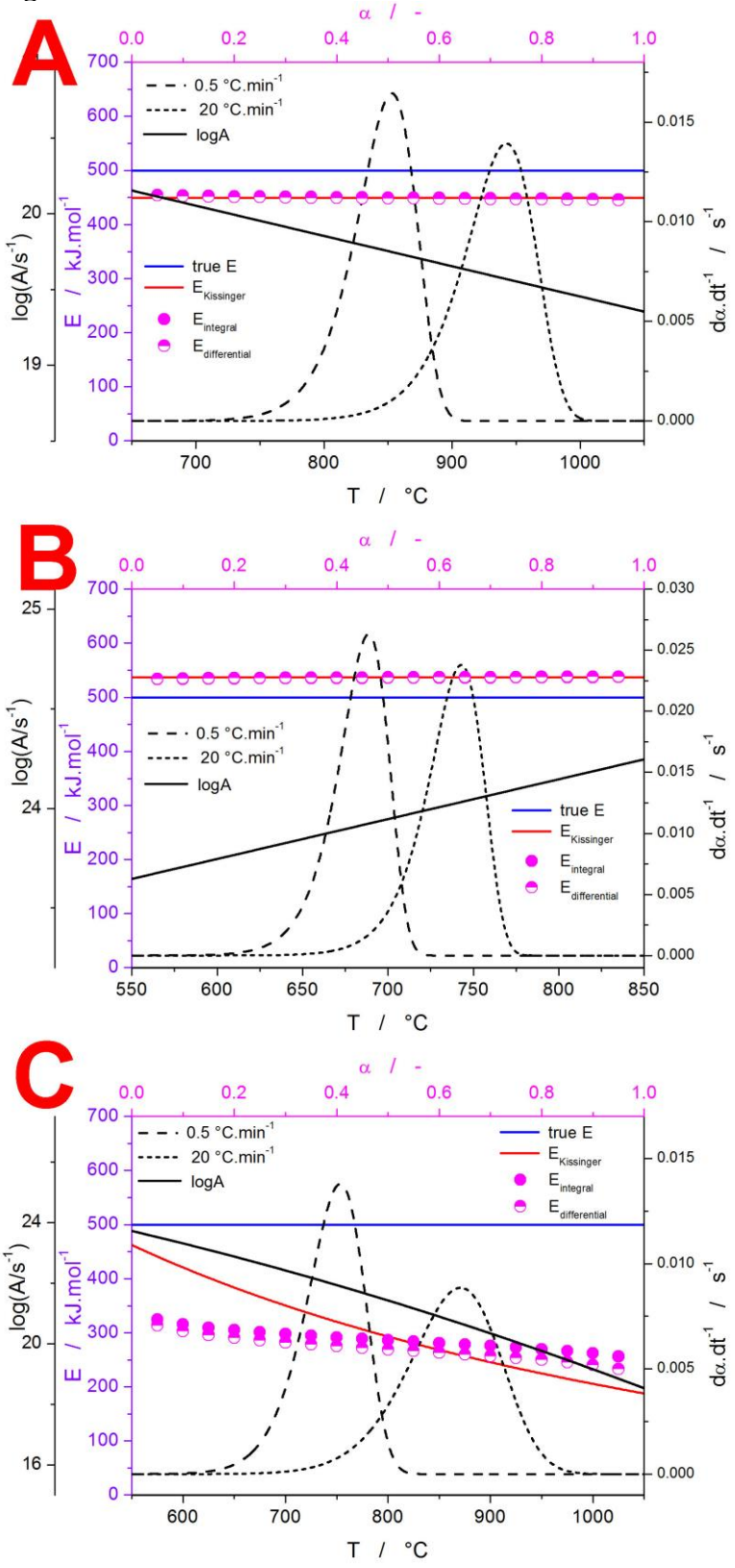
A
α / -
0.0
0.2
0.4
0.6
0.8
1.0
0.5 °C.min-1
20 °C.min-1
logA
true E
EKissinger
Eintegral
Edifferential
log(A/s-1)
E / kJ.mol-1
dα.dt-1 / s-1
T / °C
B
C

Fig. 13

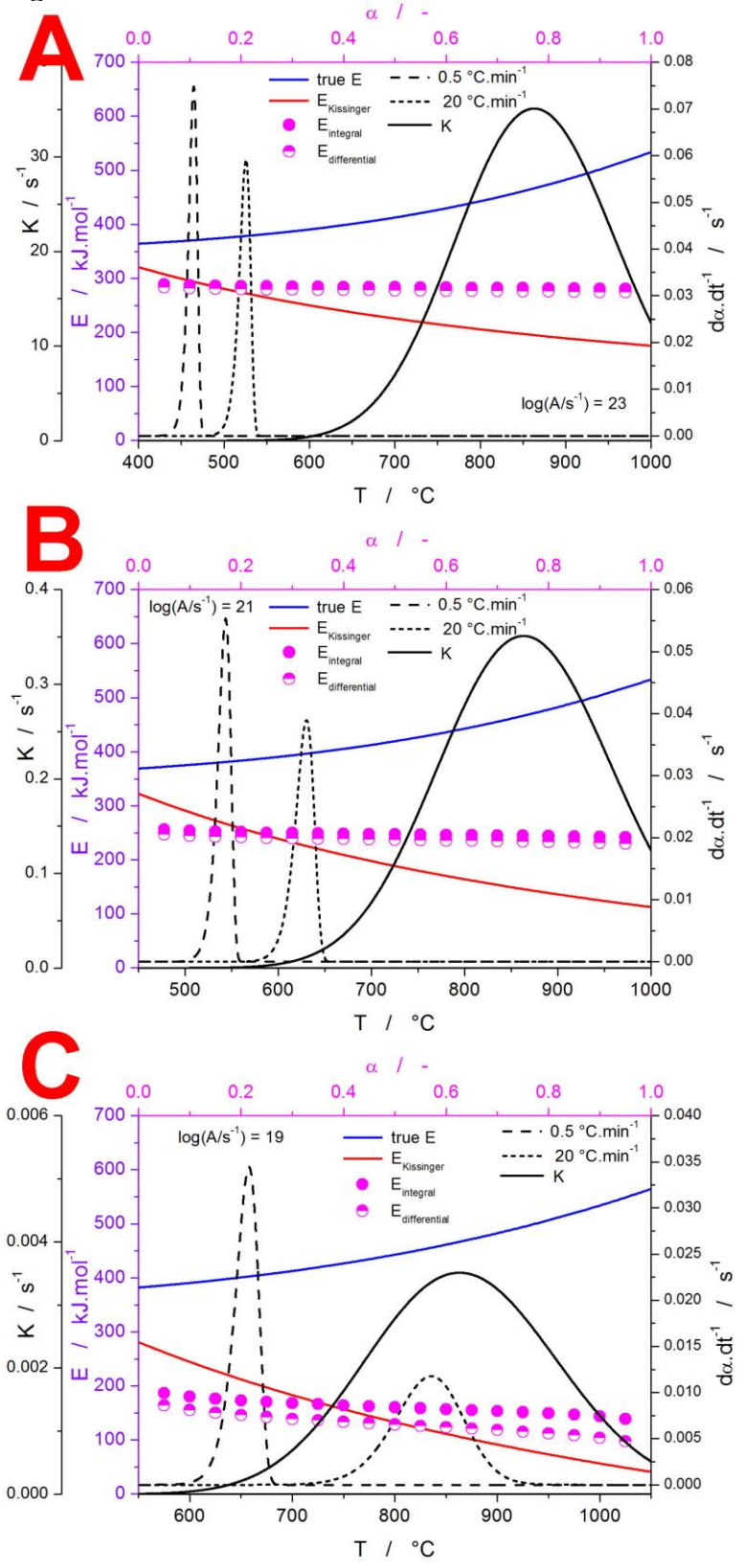
A
α / -
0.0
0.2
0.4
0.6
0.8
1.0
true E
E Kissinger
E integral
E differential
0.5 °C.min-1
20 °C.min-1
K
log(A/s-1) = 23
K / s-1
E / kJ.mol-1
dα.dt-1 / s-1
T / °C
B
log(A/s-1) = 21
C
log(A/s-1) = 19

Fig. 14

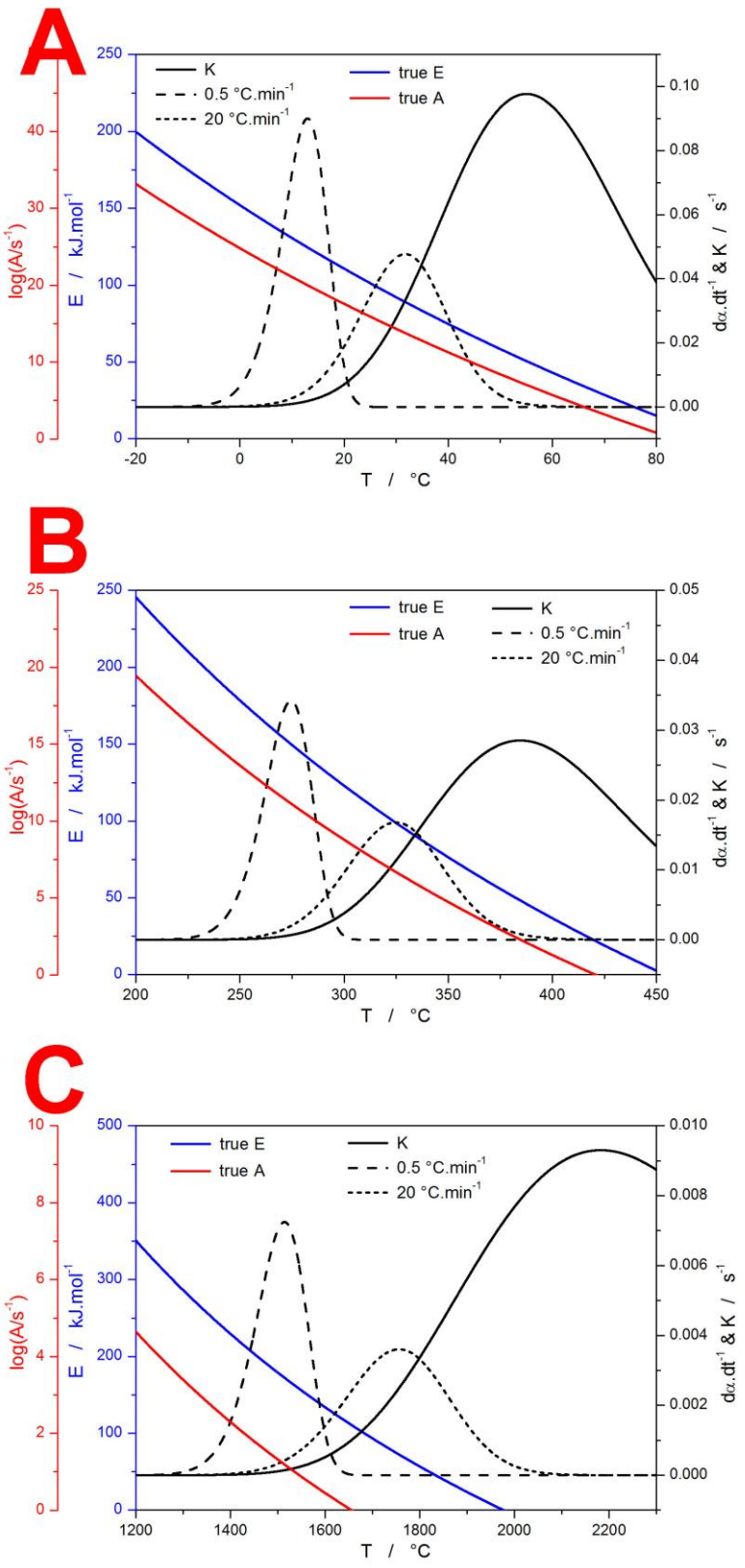
A
K
0.5 °C.min-1
20 °C.min-1
true E
true A
log(A/s-1)
E / kJ.mol-1
dα.dt-1 & K / s-1
T / °C
B
true E
true A
K
0.5 °C.min-1
20 °C.min-1
log(A/s-1)
E / kJ.mol-1
dα.dt-1 & K / s-1
T / °C
C
true E
true A
K
0.5 °C.min-1
20 °C.min-1
log(A/s-1)
E / kJ.mol-1
dα.dt-1 & K / s-1
T / °C